

# Detection of Reflected Cherenkov Light from Extensive Air Showers in the SPHERE Experiment As a Method of Studying Superhigh Energy Cosmic Rays<sup>1</sup>

**R. A. Antonov<sup>a</sup>, T. V. Aulova<sup>a</sup>, E. A. Bonvech<sup>a</sup>, V. I. Galkin<sup>a, b</sup>, T. A. Dzhatdoev<sup>a</sup>,  
 D. A. Podgrudkov<sup>a, b</sup>, T. M. Roganova<sup>a</sup>, and D. V. Chernov<sup>a, \*</sup>**

<sup>a</sup>*Skobeltsyn Institute of Nuclear Physics, Moscow State University, Moscow, 119992 Russia*

<sup>b</sup>*Department of Physics, Moscow State University, Moscow, 119991 Russia*

*\*e-mail: chr@dec1.sinp.msu.ru*

**Abstract**—Although a large number of experiments were carried out during the last few decades, the uncertainty in the spectrum of all nuclei of primary cosmic rays (PCRs) with superhigh energies is still high, and the results of many experiments on nuclear composition of PCRs are contradictory. An overview of the SPHERE experiment on detecting Vavilov–Cherenkov radiation from extensive air shower (EAS) reflected from a ground snow surface is given. A number of experimental studies implementing this method are presented and their results are analyzed. Some other popular methods of studying PCRs with superhigh energies ( $E_0 > 10^{15}$  eV) and their main advantages and drawbacks are briefly considered. The detecting equipment of the SPHERE-2 experiment and the technique of its calibration are considered. The optical properties of snow, which are important for experiments on reflected Cherenkov light (CL) from EAS, are discussed and the history of observing reflected EAS CL is described. The algorithm of simulating the detector response and calculating the fiducial acceptance of shower detection is described. The procedure of processing the experimental data with a subsequent reconstruction of the spectrum of all PCR nuclei and analysis of the mass composition is shown. The first results of reconstructing the spectrum and separating groups of cosmic-ray nuclei with high energies in the SPHERE-2 experiment are presented. Main sources of systematic errors are considered. The prospects of developing the technique of observation of reflected EAS CL in future experiments are discussed.

**DOI:** 10.1134/S1063779615010025

CONTENTS				
Introduction	61			65
1. Method of Studying Superhigh Energy Cosmic Rays	62	3.2. SPHERE-1 Setup		65
1.1. Methods Based on Detecting EAS Particles	62	3.2.1. Design of the SPHERE-1 Setup		65
1.2. Methods Based on Detecting EAS Radiations	62	3.2.2. Results of the SPHERE-1 Setup Operation		66
1.3. Some General Remarks on Observations Results	63	4. Experiments on the SPHERE-2 Setup		67
2. History of Development of the Method	63	4.1. Geometry of the Experiment		67
2.1. The First Measurements	64	4.2. Design of the SPHERE-2 Setup		68
2.2. Development of the Method	64	4.2.1. Optical Scheme		68
3. Initial Stages of the SPHERE Experiment	64	4.2.2. Electronic Equipment		68
3.1. Prototype of the SPHERE Setup	64	4.3. Series of Measurements on the SPHERE-2 Setup		70
3.1.1. Prototype Design	64	4.4. Estimation of the Detection Accuracy and Detector Calibration		71
3.1.2. Results of the Prototype Operation	65	4.4.1. Consideration of Distortions in Signal Digitization		71
		4.4.2. Consideration of Photomultiplier Nonlinearity		72
		4.4.3. Relative Calibration		73
		4.4.4. Absolute Calibration		74
		5. Simulation and Data Analysis		75
		5.1. Model of Detector Response		75

<sup>1</sup> Enhanced version of the report at the VI Cherenkov Readings “New Methods in Experimental Nuclear and Particle Physics”, Moscow, Lebedev Physical Institute (Russian Academy of Sciences), April 9, 2013.

5.1.1. Model of the Spatial and Temporal Structure of EAS CL	75
5.1.2. Simulation of the Optical-System and Photomultiplier Responses	75
5.1.3. Simulation of the Electronics Response	76
5.2. Calculation of the Fiducial Acceptance	76
5.2.1. Simulation of the Trigger Response	76
5.2.2. Calculation of the Acceptance for Discrete Values of the Altitude	77
5.3. Estimation of the Accuracy of the Acceptance Calculation	77
5.4. Reconstruction of SDF of Experimental Events	78
5.5. Estimation of the Energy of Primary Nuclei	80
5.6. Procedure of Reconstructing the Spectrum of All Nuclei	80
5.7. Separation of PCR Nuclear Groups	81
6. Results of the SPHERE-2 Experiment	82
6.1. Energy Spectrum	82
6.2. Estimation of the PCR Composition	82
7. Prospects of Developing the SPHERE Experiment	83
7.1. Problems for New Experiments	83
7.2. Design of the High-Definition SPHERE-HD Setup	83
7.3. Project of Technique Application in Antarctica	84
Conclusions	84
References	85

gies are currently carried out by indirect methods according to the characteristics of extensive atmospheric showers (EAS) (cascades of secondary particles generated by PCR particles in the Earth atmosphere). There are strong fluctuations of the EAS parameters, which are mainly determined by the development of hadronic cascade generating all other EAS components. Therefore, the results of analyzing the experimental data depend on the properties of nucleus–nucleus interactions at superhigh energies remaining unknown so far.

Detectors of PCRs with superhigh energies detect various EAS components: electron–photon, muon, hadron, fluorescent radiation, Vavilov–Cherenkov radiation, etc. In this paper, we present an overview of a relatively new technique of studying PCRs: detection of optical Vavilov–Cherenkov radiation, which is more often referred to as Cherenkov light from EAS (EAS CL), reflected from a snow surface. This approach has several advantages:

(i) A large EAS CL detection area can be provided using a compact device.

(ii) Fields of view of individual sensing elements of the device cover a significant part of the area of observation surface, which makes it possible to observe EAS CL directly in the paraxial shower region, which is generally inaccessible for ground-based detectors.

(iii) A possibility of changing the detector altitude allows one to analyze the same fragments of the PCR spectrum with different resolutions (distances between the centers of fields of view of neighboring sensing elements) to control the values of systematic effects.

When implementing the method of detecting reflected EAS CL, the properties of snow surface are of great importance. The results of studying the optical properties of snow were published repeatedly by several research groups [7–9].

The simulation results reported in [8] show that the relative reflection coefficient for pure snow is stable (within 3%) for zenith angles of a light source from  $0^\circ$  to  $80^\circ$  in the wavelength range of 300–600 nm. It can be concluded based on the reported results and the known CL spectral characteristic [10] that a snow surface reflects CL with small spectral distortions at zenith angles up to  $80^\circ$  and can be used as a screen when detecting EAS CL.

In comparison with ground-based Cherenkov systems detecting direct CL from showers, a snow surface makes it possible to exclude the influence of light reflection from the glass of photomultipliers. To measure light flux, many modern devices are equipped with the so-called “cosine head” [11] made of a semi-transparent opaque material. This head scatters the incident photon flux, thus making it possible to exclude the influence of the dependence of the coefficient of reflection from the surface of device optical elements on the angle of radiation incidence [11, 12].

## INTRODUCTION

Cosmic rays (CRs)—particles accelerating in active objects of various natures and filling the Galaxy and extragalactic space—may be an important factor of space-system dynamics [1]. Remote methods of studying CRs in order to obtain information about CRs far from the Earth are still important. For example, observations of molecular clouds by the FERMI-LAT  $\gamma$  telescope [2] can be used to reconstruct the shape of primary cosmic rays (PCRs) spectrum beyond the Solar System [3, 4]. Nevertheless, the main source of information about PCRs is their near-Earth detection.

The PCR energy spectrum extends in energy for no less than 12 orders of magnitude (from  $10^9$  to  $10^{21}$  eV) and sharply decays with the increase in energy. PCR particles with energies up to  $10^{15}$  eV can be detected by direct methods using detectors mounted on spacecrafts and high-altitude balloons [5, 6]. The intensity of particles with superhigh energies (above  $10^{15}$  eV) is so low that all investigations on PCRs with such ener-

When detecting EAS CL reflected from the snow surface, snow serves as a “cosine head”. Therefore, this detection method allows one to measure the CL density with a high accuracy.

Peculiar features of detecting various EAS components, ranges of application of the corresponding experimental methods, and their typical advantages and drawbacks are briefly considered in Section 1. The history of development of the method of observing reflected EAS CL is described in Sections 2 and 3. Currently, the most reliable results obtained by the method of detecting reflected EAS CL are provided by the SPHERE-2 setup. The setup equipment, detector calibration methods, and observation results obtained by the SPHERE-2 setup are considered in Section 4. Simulation of the detector response and algorithms of data analysis are described in Section 5; the results obtained are given in Section 6. Finally, possibilities of further development of the method of observing reflected EAS CL are discussed in Section 7.

## 1. METHOD OF STUDYING SUPERHIGH ENERGY COSMIC RAYS

The EAS components can be divided into two large groups: cascade particles (hadrons, muons, electrons, and gamma quanta) and radiations accompanying the cascade development (Cherenkov light, fluorescent light (FL), radio emission, microwave radiation, and acoustic effects). Large modern detectors as Pierre Auger Observatory (Auger) [13], Telescope Array (TA) [14], Yakutsk EAS Array (Yakutskaya Ustanovka) [15, 16] are hybrid (i.e., they detect various EAS components).

### 1.1. Methods Based on Detecting EAS Particles

Observation of EAS charged components is one of the oldest and most elaborated methods of studying PCR spectra. A kink in the PCR spectrum at energy of  $\sim 3 \times 10^{15}$  eV (the so-called “knee”) was found in specifically the distribution over the number of charged particles in a shower [17]. The vast majority of high energy EAS charged particles are electrons and positrons. EAS electrons can be detected using various experimental methods. To this end, Geiger–Mueller counters were initially applied (for example, in the ShAL MGU system) [17]. Currently, scintillation detectors (KASCADE-Grande [18], AGASA [19], and TA [20]) are most popular. In the Auger experiment, the EAS charged component is detected by 1600 water tanks (the area of each tank is  $12 \text{ m}^2$ ) [21].

Detection of the EAS charged component is independent of the atmosphere transparency and the level of background illumination and provides almost continuous system operation, which is a great advantage for studying the shape of the spectrum and anisotropy of PCRs [22]. The shape of spatial distribution func-

tion (SDF) of shower electrons can, in principle, be used for analyzing the PCR nuclear composition [23].

At the same time, EAS development depends on the atmosphere density profile, and only the particles that reached the Earth surface can be observed. The shape of SDF of shower electrons can generally be determined with only a large error, which reduces the sensitivity of this value to the PCR nuclear composition. Therefore, to analyze the PCR nuclear composition, a combination of two parameters is generally used: measured numbers of electrons ( $N_e$ ) and muons ( $N_\mu$ ) in shower (or the corresponding “reduced” values in a circle or ring centered at the shower axis) [24]. The number  $N_\mu$  of muons in shower is small in comparison with  $N_e$  and, therefore, difficult to measure accurately. In addition, the calculated  $N_\mu$  value depends especially strongly on the model of nucleus–nucleus interaction at superhigh energies [25], which significantly hinders the analysis of the PCR nuclear composition by the above method. In turn, the  $N_e$  value, which is often used as a measure of primary-particle energy, also depends on the PCR composition, thus leading to an additional systematic error of the measured spectrum for all nuclei.

### 1.2. Methods Based on Detecting EAS Radiations

Since each shower electron having a sufficiently high energy (above 22 MeV at sea level) generates many Cherenkov photons, the total EAS CL flux is approximately proportional to the energy of primary particle that formed EAS. However, the total CL flux cannot be directly measured by ground-based systems: only the Cherenkov photon flux density in setup detectors, which are generally spaced by rather large distances (tens or hundreds of meters), is measured. Using the calculated SDFs, one can estimate the total EAS CL flux and the primary-particle energy.

Nevertheless, the shape of the SDF of EAS CL can be reconstructed with a smaller error as compared to the shape of the SDF of shower electrons, which simplifies the analysis of the PCR composition by Cherenkov methods. Thus, there is a fundamental possibility to weaken the dependence of the measured spectrum of all nuclei on the PCR composition, provided that the information about the shape of the SDF of EAS CL is taken into account. This possibility was successively implemented for the first time in studies of the SPHERE collaboration (see Section 5 for more details).

EAS charged particles pass through the atmosphere to excite nitrogen molecules. Removing this excitation, nitrogen molecules isotropically emit FL detected in modern setups (Auger [13], TA [14], and HiRes [26]) using telescopes. Since electrons are the main EAS charged component near the shower maximum and their spatial arrangement is so that a half of all electrons are spaced by no more than 140 m from

the shower axis, the shower image at the telescope photomultiplier matrix appears as a line of variable brightness (i.e., the shower cascade curve is recorded). The primary-particle energy and type are reconstructed (based on the data of fluorescent telescopes) using the cascade-curve shape and the depth  $X_{\max}$  of cascade maximum.

The method of the depth of maximum is also most popular for studying the PCR nuclear composition using the Cherenkov technique (see [25]). The parameter  $X_{\max}$  is not measured directly in Cherenkov experiments; however, it can be estimated proceeding from the statistical dependences of the SDF slope of EAS CL (ratio of the integrals of the total number of Cherenkov photons in rings with different radii) or the EAS CL pulse waveform at some distance from the shower axis on the depth of cascade maximum.

Unfortunately, EAS CL and FL can be observed at only clear moonless nights, which represent no more than 5–10% of all time; this is the main drawback of optical methods of detecting EAS. In contrast to CL, EAS FL has no directionality, and its yield is lower as compared with CL; therefore, the fluorescent-detector threshold is generally no less than  $3 \times 10^{17}$  eV.

Currently, the method of observing and analyzing EAS radio signal is very intensely developed [27]. At the same time, the sensitivity of radio signal to the PCR nuclear composition has been convincingly confirmed only recently [28]. In addition, it should be noted that the threshold of reliable observation of EAS radio signal is fairly high (for example, characteristics of events with energies above  $5 \times 10^{16}$  eV were considered in [27]); therefore, the radio method, being relatively inexpensive, is most promising for extremely high energies. Studies on detecting microwave [29, 30] and acoustic EAS radiations [31] are at even earlier stage of development.

### 1.3. Some General Remarks on Observations Results

To date, there are several tens of measurements of the spectrum and investigations of the PCR nuclear composition for different EAS components carried out in the region of superhigh energies. The results of relatively recent experiments on the spectrum of all nuclei were given in [15, 16, 18, 32, 33]. Although the spectra of all nuclei obtained for the last two years by large setups are in good agreement with each other [34], the difference in the results of some other experiments has a large magnitude and often exceeds the range of specified uncertainties. For example, the spectrum obtained in the GAMMA experiment [35] has a statistically significant (more than  $4\sigma$ ) sharp peak at energy of  $8 \times 10^{16}$  eV, which is absent in the data obtained by other experiments (Akeno [36], Tibet-III [37], and KASCADE-Grande [18, 38]). This peak is observed in the spectrum obtained in the Tunka-133 experiment during the 2009–2010 season

[39] but is absent in the spectrum obtained during the 2010–2011 season [40].

Concerning the PCR nuclear composition, most experiments provide only estimates of the mean logarithm of the mass number  $\langle \ln A \rangle$  without separation of nuclei into groups [24, 26, 41–44]; the spread of the measured  $\langle \ln A \rangle$  values is rather large [25]. Recent results obtained in the KASCADE-Grande experiment [45], where the spectra of “light” (mainly  $p$  and He) and “heavy” (CNO, Si, and Fe nuclear groups) components were separately recorded, are unexpected because the transition to extragalactic sources was found to be smooth. Even at energy of  $10^{18}$  eV the fraction of heavy nuclei is large, which is in poor agreement with the results of HiRes [46], TA [14], and Auger [13]. In any case, the presence of a significant (more than 50%) light-component fraction in the PCR composition at energy above  $10^{18}$  eV (which does not contradict results of the latest experiments) causes serious difficulties in one of the most popular models of the transition from galactic sources to an extragalactic, “ankle” model [47], because PCR anisotropy is too high in some galactic models [48] and contradicts the results of Auger [22, 49].

These considerations demonstrate that the investigations of the spectrum and composition of superhigh energy cosmic rays by different methods should be continued. Similar considerations were reported earlier [50–56]. It can be seen that the experimental situation has only slightly changed since 2008. In the last three studies, a new technique of investigating the PCR composition based on the spatial–angular distribution (SAD) of EAS CL, which can radically improve the separability of PCR nuclear groups, was developed. Until this technique is implemented, the shape of the SDF of EAS CL remains one of the best indicators of the PCR mass composition.

## 2. HISTORY OF DEVELOPMENT OF THE METHOD

The method of detecting CL (reflected from a snow surface) from EAS generated by superhigh energy cosmic rays was first proposed by Chudakov [57]. It was proposed to mount two photomultipliers and two electro-optical converters (EOCs) with identical opening angles of  $\pm 45^\circ$  on a plane board. All four devices should observe the snow-covered ground surface from an altitude of about 10 km. A simultaneous response of amplitude discriminators of the two photomultipliers was assumed to be the condition for triggering shutters of cameras mounted on EOCs. A subsequent processing of images of EAS Vavilov–Cherenkov radiation spots in photographs should provide the information about the energy and arrival direction of a primary space particle.

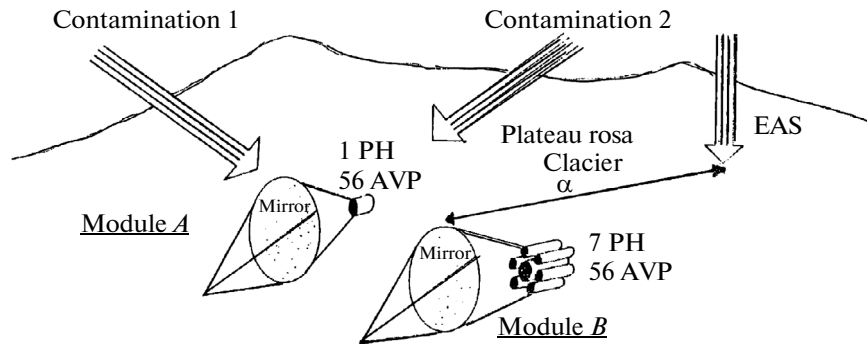


**Fig. 1.** Schematic view of the experiment carried out by Navarra in the Alps at an altitude of 3500 m. The figure is taken from the original paper published in 1981 [58].

### 2.1. The First Measurements

The first attempt to carry out measurements by this technique was made by Navarra et al. [58] in the late 1970s–early 1980s in Italy. The measurements were performed using four parabolic mirrors  $0.6 \text{ m}^2$  in area with either one or seven photomultipliers (connected in parallel) in the focus of each mirror (Fig. 1). The experiment was carried out in mountains at an altitude of 3500 m above sea level. Detectors with opening angles of  $3^\circ$  were placed at a distance of 1000 m from the glacier and observed a region 27.5 m in radius. Various configurations of the setup were investigated. The result of the study was the integral spectrum, in which the intensity of events corresponded to the expected one. Further studies using this technique did not follow.

### 2.2. Development of the Method

At the same time, Antonov et al. [59–61] proposed the use of a Schmidt optical system composed of a spherical mirror with a photomultiplier placed in the focus and a correcting diaphragm. An advantage of this system is a large (up to 1 sr) opening angle at a high illuminance, which makes it possible to observe a large

area. When the number of photomultipliers in the mirror focus is sufficiently large, the images of light spots can be analyzed without EOCs. In addition, it was proposed in these works to use a balloon for lifting the system above a snow-covered surface. This technique is implemented in the SPHERE experiment.

It is planned to carry out the SPHERE experiment in three stages. In the first stage, where the device is lifted to an altitude up to 1000 m by a captive balloon, the measurement technique is worked through; the possibility of reducing the energy threshold, the nature of background events, and the spatial and temporal characteristics of detected showers are studied; and the energy spectrum is measured at energies above  $10^{16} \text{ eV}$ . In the second stage, the energy spectrum is investigated at energies up to  $10^{18} \text{ eV}$  and the device is lifted to an altitude up to 3 km. In the third stage, it is planned to study the energy spectrum at energies up to  $10^{20} \text{ eV}$  during a long-term balloon flight above Antarctica in winter at an altitude of 30–40 km.

While we are writing this review, the first stage of carrying out the experiment is at its end.

## 3. INITIAL STAGES OF THE SPHERE EXPERIMENT

### 3.1. Prototype of the SPHERE Setup

In the early 1990s, the first measurements of the PCR energy spectrum using a prototype of the SPHERE setup were carried out in the Tien Shan Mountains. Being mounted on a mountain slope, the setup observed the snow-covered ice on the surface of the Big Almaty Lake (Fig. 2).

**3.1.1. Prototype design.** The optical equipment of the system included a spherical mirror 1.2 m in diameter with the radius of curvature of 0.75 m, a diaphragm with the window diameter of 0.8 m, and a mosaic array of 19 photomultipliers (FEU-110) [62] located in the mirror focus.

Electronics of the system included 20 independent detection channels (one of them is reserve) digitizing the anode current of photomultipliers. The detection

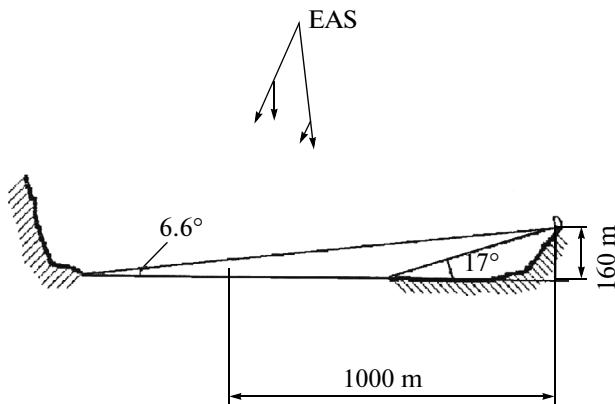


**Fig. 2.** Geometry of the experiment with the prototype of the SPHERE setup at the Big Almaty Lake.

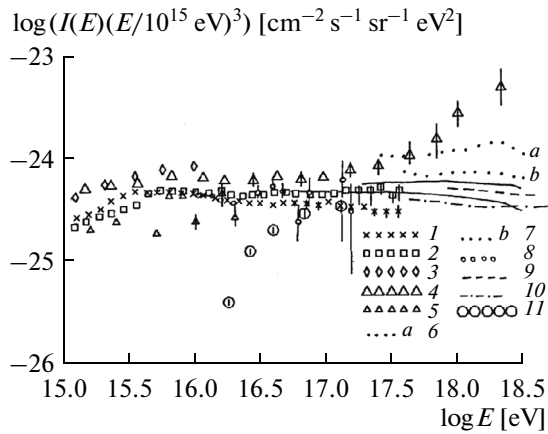


**Fig. 3.** Differential energy spectrum based on data of the prototype of the SPHERE setup (1996). (1) MGU [63], (2) Akeno [36, 64], (3) Tien Shan [65], (4) Tien Shan [65], (5) Samarkand [66], (6) Yakutsk85 [67], (7) Yakutsk91 [67], (8) Yakutsk [68], (9) Haverah Park [69], (10) Fly's Eye [70, 71], and (11) SPHERE [72].

process was triggered by a master board when one of the following conditions is valid: amplitude of a photomultiplier anode pulse exceeds some threshold level in any photomultiplier (Master M1) or amplitudes in two neighboring photomultipliers, one of which is in the central horizontal row, exceed a specified level (Master M2). This condition was due to the fact that only photomultipliers in the central row were oriented directly to the lake. After the end of digitization, the information was transferred to a control computer through a cable and stored.

Direct current of a FEU-110 photomultiplier is proportional to the average illuminance of photocathodes by a stellar sky background. The constant component of photomultiplier anode currents was periodically measured during the experiment, which made it possible to monitor atmosphere transparency during the measurements.

**3.1.2. Results of the prototype operation.** The result of the measurements carried out using the prototype of the SPHERE setup is the PCR energy spectrum (Fig. 3) obtained for the first time by the method of detecting CL reflected from a ground snow surface. A complex geometry of the experiment shown in Fig. 4 led to an increase of the threshold region for the recorded spectrum. Nevertheless, two spectral points are in good agreement with the results of other experiments [73] at energies of about  $10^{17}$  eV.

The experimental results confirmed that this method can be used to measure the energy spectrum and laid a foundation for its further development.

### 3.2. SPHERE-1 Setup

In the late 1990s, the SPHERE-1 balloon setup was designed. The electronic equipment was supplied

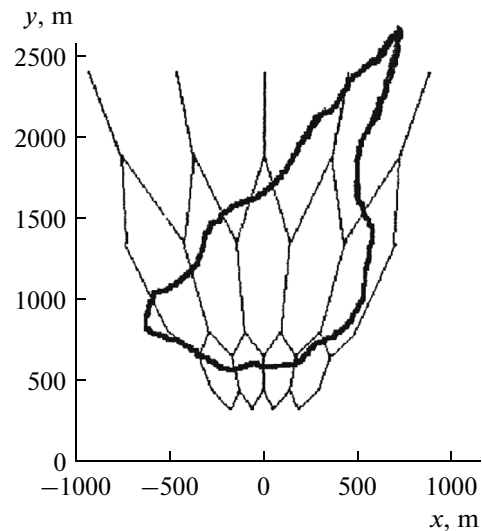


**Fig. 4.** Contour of the lake with indicated areas observed by several central photomultipliers in the array.

with an instrument for measuring the photomultiplier pulse widths and an on-board computer. The power consumption was reduced to 30 W, which made it possible to supply the equipment by accumulators and lift it by a captive balloon to an altitude up to 1000 m.

**3.2.1. Design of the SPHERE-1 setup.** Figure 5 shows the optical equipment of the system consisting of a spherical mirror 1.2 m in diameter with an array of 19 photomultipliers (FEU-110) in the focal plane and a correcting diaphragm 0.8 m in diameter. Being lifted to an altitude of 1 km, each photomultiplier observed an area about 200 m in diameter.

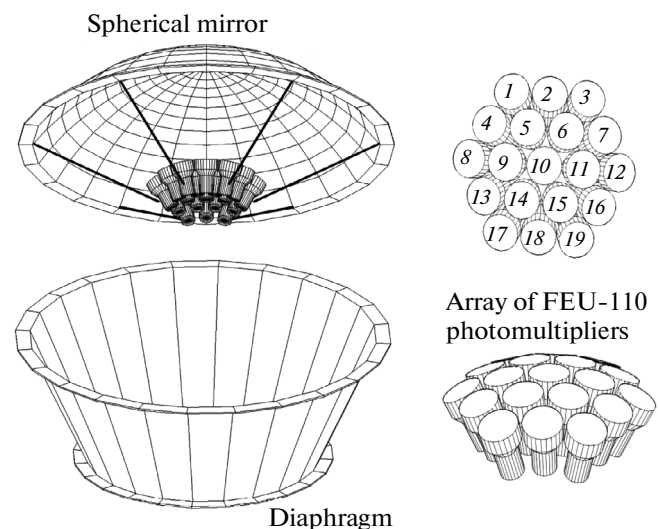


**Fig. 5.** Schematic layout of the optical system of the SPHERE-1 setup.

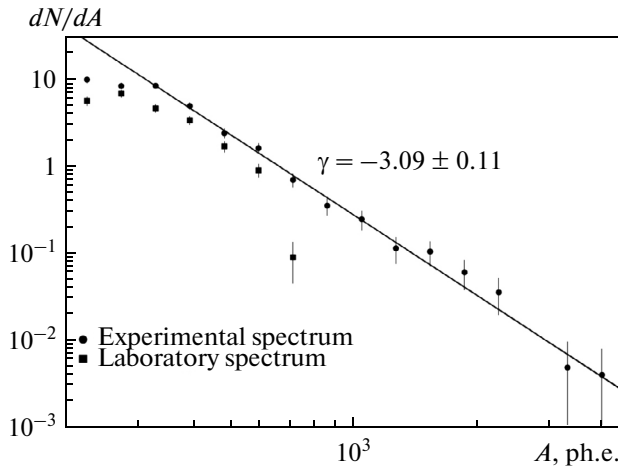


**Fig. 6.** Differential spectra based on the experimental and laboratory data with an equivalent background-light level.

The system worked in one of two measurement modes. In the Master M2 mode, the trigger condition was simultaneous exceeding of a discriminator threshold by pulse height in any two photomultipliers of the array; in the Master M1 mode, exceeding a threshold in any photomultiplier was sufficient. When the trigger condition is satisfied, the anode-pulse charge, as well as the instants of pulse beginning and end, were recorded in each photomultiplier for  $2.0 \mu\text{s}$  with a step of  $30 \text{ ns}$ .

The operation of electronics was automatically controlled by the on-board computer. A high voltage power supply for photomultipliers and discriminator thresholds were set by the computer software proceeding from current and maximum allowable photomultiplier currents. Photomultiplier currents, supply voltage from accumulators, and temperature in the container with electronics were constantly monitored. The stability of photomultiplier amplification was controlled as follows: light pulses with different intensities from a LED were periodically fed to each photomultiplier through optical fibers. Data were recorded on the on-board computer hard drive.

The system was lifted several times using an AZ-55 balloon at the Lyagoshi military ground spaced by  $30 \text{ km}$  from Vol'sk town (Saratov region) in 1997–2000. The energy spectrum in the energy range of  $10^{16}$ – $10^{17} \text{ eV}$  was measured for the first time during the observation sessions in 1997 and 1998 [74]. UFS-1 UV filters  $6 \text{ mm}$  thick [75] were used in these measurements to suppress the stellar light background. However, the experimental data were noisy because of background events caused by detection of flashes from particles passed through filters and photomultiplier glass of the detector. The measurements in 2000 were performed without filters, and the number of background events decreased, thus increasing the fraction of events recorded from EAS.

Several next years were devoted to preparation for launches of the SPHERE-1 setup by a balloon in Antarctica during the polar night. It was assumed that the exposure time of the system would be several hundreds of hours. The system was brought to the Novolazarevskaya Russian Antarctic station to measure the stellar background near the station. Unfortunately, in 2004, when the balloon was released, the rope holding the system broke, and the SPHERE-1 setup was lost.

**3.2.2. Results of the SPHERE-1 setup operation.** In 2000, about 400 events caused by EAS CL were detected during ten-hour flight of the SPHERE-1 setup on a captive balloon at an altitude of  $900 \text{ m}$ . The processing of the experimental data allowed one to obtain for the first time images of EAS CL flashes on a snow “screen”. The results obtained were used to construct the PCR spectrum in the range of  $10^{16}$ – $10^{17} \text{ eV}$  [76].

The measurement time interval was 457 minutes (164 minutes in the Master M1 mode and 293 minutes in the Master M2 mode). The system detected 228 327 and 102 239 trigger responses, respectively. The overwhelming majority of events were due to fluctuations of the stellar-sky light background; their value was about 100 photoelectrons per detector for  $2 \mu\text{s}$ . An analysis of the obtained data showed that events caused by both stellar sky and technogenic reasons barely contain pulses wider than  $30 \text{ ns}$ , which makes it possible to effectively filter out these events. Points in Fig. 6 show the spectrum of pulses selected according to the criterion of pulse duration. Squares indicate the laboratory spectrum with the light background equal to that in the experiment. The sums of photoelectrons detected by three photomultipliers with the largest amplitudes are plotted on the abscissa axis. When passing from this spectrum to the energy spectrum of cosmic particles, the simulation results were taken into account [74, 77].

The obtained PCR energy spectrum is compared with the data of the Tunka-25 experiment in Fig. 7 [78]. These results are consistent within statistical errors. The spectrum exponent is  $\gamma = -3.09 \pm 0.11$ .

The possibility of reconstructing shower parameters, which include the coordinates and angle of inclination of the axis, as well as the shape of the SDF of CL, was analyzed based on the shape of light-spot image on the photomultiplier array (Fig. 8).

Only 19 of 44 events with energy above  $3 \times 10^{16} \text{ eV}$ , the axes of which fell in the central part of the field of view of the system, were selected. The position of the shower axis in an event was found according to the “centroid” of the image observed. The arrival direction and the shape of the SDF of CL were determined by the method of  $\chi^2$  minimization. CL SDF was taken in the form:

$$Q(R) = A \left( 1 + \frac{R}{R_0} \right)^{-4.3}, \quad (1)$$

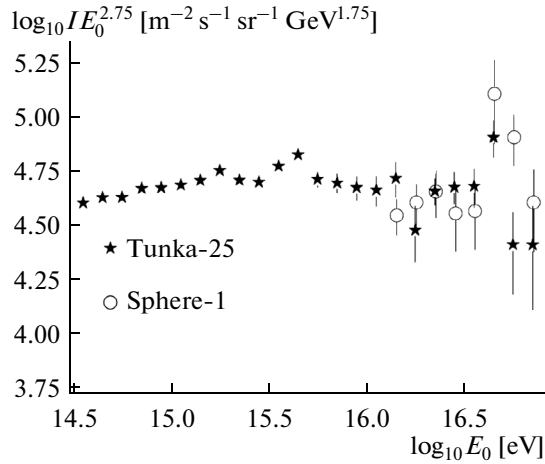


**Fig. 7.** PCR energy spectrum according to the data obtained by the SPHERE-1 setup in 2001.

where  $R_0$  is the shower parameter and  $R$  is the distance from the shower axis. An accuracy of the reconstructed parameters was estimated based on the processing of a sample of simulated events. For events with energy of about  $3 \times 10^{16}$  eV, sets (each containing 50 events) with zenith angles  $\theta = 8^\circ, 25^\circ, 40^\circ$ , and  $60^\circ$  were simulated. The  $R_0$  value was assumed to be 200 m. The results of the processing are shown in Table 1.

For events detected in the experiment, the mean values of zenith angle and  $R_0$  were  $37^\circ$  and 325 m, respectively. The shape of average CL SDF measured in Yakutsk for EAS with zenith angles ranging from  $0^\circ$  to  $30^\circ$  [79] is described by expression (1) with the parameter  $R_0$  of about 200 m, which gradually increases with an increase in the EAS zenith angle.

Thus, the experimental data on the PCR energy spectrum and parameters of individual EASs obtained by the SPHERE-1 setup are in agreement with the known data in this field.

#### 4. EXPERIMENTS ON THE SPHERE-2 SETUP

A further progress in developing this method is due to an upgrade of the system and regular lifting of the system in more favorable climatic regions.

##### 4.1. Geometry of the Experiment

The SPHERE-2 setup was designed to be lifted to an altitude up to 1 km by a captive balloon at nighttime (Fig. 9). The system operates like a video camera and records the dynamics of light spots formed by EAS CL on a snow-covered ground surface.

The balloon was released from an equipped ground on the Lake Baikal ice (Fig. 10). The optical properties of snow were studied at the place where the measurements were carried out. Figure 11 shows the dependence of the relative reflection coefficient on the angle between the optical axes of light source and luxmeter.

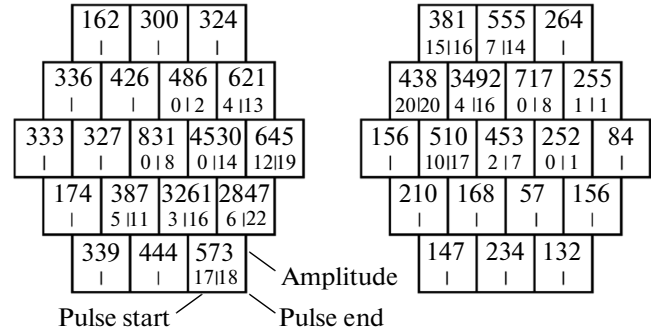


**Fig. 8.** Example of two detected events. The charge amplitude for 2  $\mu$ s is in photoelectrons and times are in code units for 30 ns. A typical diameter of the ground surface area observed by one detector is 200 m.

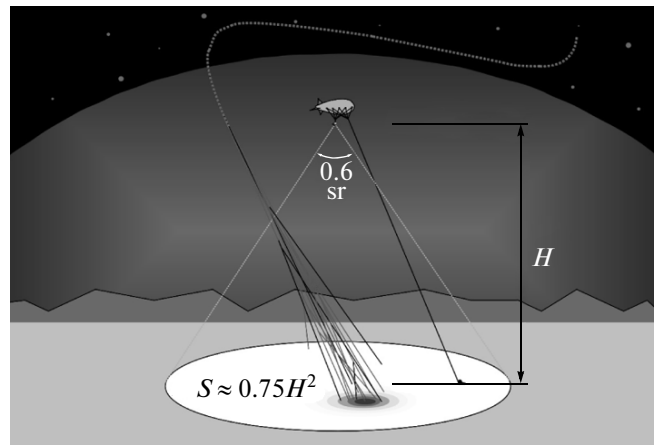


**Fig. 9.** Schematic view of the experiment with the SPHERE-2 setup.

A collimated LED beam formed (being vertically oriented) a spot of  $\sim 30$  or  $\sim 50$  cm in diameter on the snow surface. The luxmeter was fixed above the observed surface at a height of 1 m. The luxmeter optical axis was oriented perpendicular to the snow surface. The scheme of measuring reflected EAS CL for the SPHERE-1 and SPHERE-2 setups was simulated in this experiment. Multiple measurements of the absolute reflection coefficient of solar light scattered from snow yielded values from 0.82 to 0.85.

**Table 1.** Estimated accuracy of reconstructing EAS parameters

Inclination of axis [deg]	8	35	60
$\sigma(\theta)$ [deg]	7	7	6
$\sigma(R_0)$ [m]	10	30	40
$\sigma(x_0, y_0)$ [m]	5	7	10
$\sigma(E_0)$ [%]	10	10	10

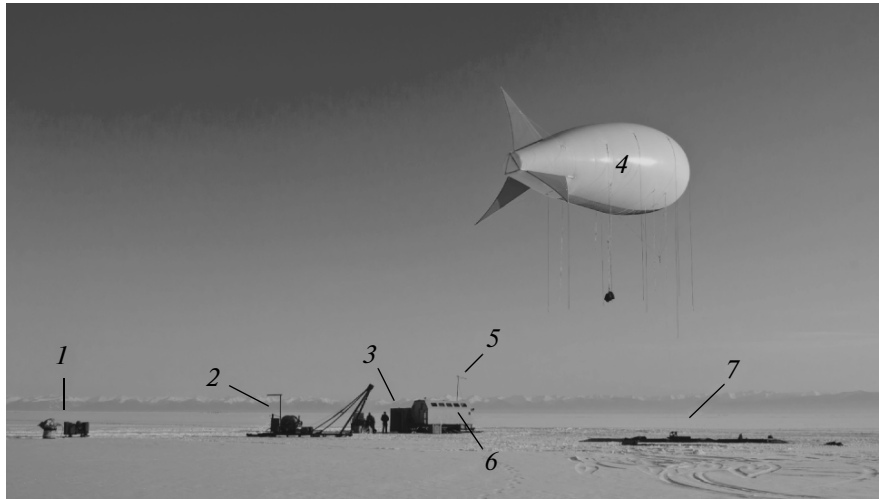


**Fig. 10.** Test release of the balloon with an equivalent load for controlling its angle of attack. The launch ground is equipped with (1) power supply cable (1 km) and reserve generator; (2) hoist; (3) container with the SPHERE-2 setup; (4) 250-m<sup>3</sup> BAPA balloon; (5) Internet-access antenna; (6) control center; and (7) load unit.

#### 4.2. Design of the SPHERE-2 Setup

Proceeding from the experience of the SPHERE-1 setup operation, it was decided to increase the aperture ratio and the spatial and temporal resolutions of the new SPHERE-2 setup in comparison with prototypes. An increase in the number of photomultipliers in the light-detector array and recording of the pulse waveform in each channel makes it possible to reduce the energy threshold, increase the accuracy of determining the shower arrival direction, and analyze SDF of EAS CL in a wide range of distances from the axis.

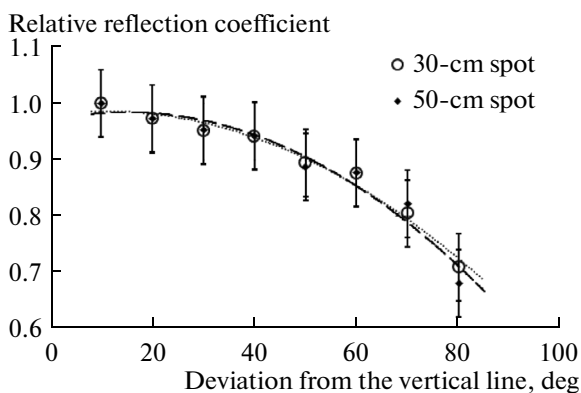


**Fig. 11.** Dependence of the relative reflection coefficient of snow surface on the zenith angle of light arrival. Unity on the vertical axis corresponds to the reflection coefficient when the light source (white LED, 440–700 nm) is vertically arranged. Diamonds and circles correspond to two independent measurements. Vertical lines at marks indicate methodical errors of the measurements.

**4.2.1. Optical scheme.** The SPHERE-2 balloon setup [50] includes a seven-segment spherical mirror 1.5 m in diameter with a radius of curvature of 0.94 m; an array of 108 FEU-84-3 photomultipliers and one Hamamatsu R3886 photomultiplier is mounted in its focus. A diaphragm 0.93 m in diameter is placed before the mirror to improve the spatial resolution. The opening angle of the optical system is 52° (Fig. 12). Each photomultiplier observes (from an altitude of 1 km) a region about 50 m in diameter on the snow-covered surface.

**4.2.2. Electronic equipment.** A container with electronic equipment mounted above the mirror of the system (Fig. 13) records a light-pulse profile in each channel for 12.8 μs with a step of 12.5 ns. Each channel includes two 40-MHz analog-digital converters with preamplifier gains of –30 and dynamic range of 10<sup>3</sup>.

Each photomultiplier is supplied by a miniature (62 × 25 × 25 mm) high-voltage power supply with 11 outputs for connecting to a photomultiplier dynode system. Each source consists of a multiplier circuit and a control board with an inductive storage unit for generating high-voltage pulses. The control is performed via I<sup>2</sup>C interface, which makes it possible to set the high voltage in the range from –800 to –1500 V and obtain the information about the anode current (with an error of 0.1 μA), high voltage (with an error of 1 V), +15 V supply voltage, and photomultiplier temperature.

To control all 109 power sources, a commutator board was designed, which allows one to commute the on-board computer and any source. The power consumption of each source does not exceed 90 mW.

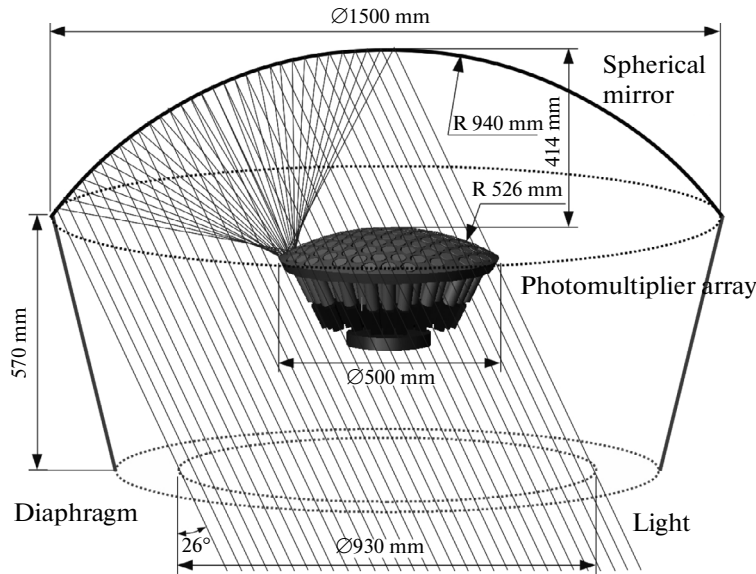


Fig. 12. Schematical layout of the optical system of the SPHERE-2 setup.

The trigger system of the setup has 112 inputs (109 primary and 3 reserve) for acquisition of the requests for sending trigger confirmation signal from the channel discriminators. The trigger board can select the events where the discriminators of neighboring photomultipliers respond in the time interval of  $1 \mu\text{s}$ . The logical model of the photomultiplier array is stored in the chip of the programmable logic device on the trigger board.

The SPHERE-2 setup is equipped with a LED calibration board. The board includes 7 independently controlled FYL-5013-VC1C LEDs with the main emission line wavelength of 405–410 nm. Each LED can be switched on at an arbitrary instant to emit with arbitrary brightness for a specified time interval. Light pulses pass through 7 optical fibers 1 mm in diameter to illuminate the photomultiplier array. The optical fibers are rigidly fixed in holes in the mirror and have diffusers at the ends for more uniform illumination of all photomultipliers.

Beginning in 2012, the following operation mode of the board was implemented. A signal from the trigger board initiates a short (100 ns) pulse at all LEDs. The signal is formed  $5 \mu\text{s}$  after triggering and recorded to the end of the event frame. This pulse is used for accurate (up to 1.2–1.4 ns) synchronization of all measuring channels. Then,  $6 \mu\text{s}$  later, LEDs are repeatedly switched on in various combinations (see Table 2), and the results are recorded in a separate calibration frame. The duration of each combination is 375 ns. The calibration-frame data make it possible to monitor the sensitivity of each photomultiplier and linearity of their characteristics. The calibration procedure is described in detail in Sections 4.4.2 and 4.4.3.

The setup is equipped with the following:

(i) GPS navigation system for determining the setup position with an error of 4–5 m with the PPS time signal for binding each event to the world time with an error of  $1 \mu\text{s}$ . The PPS signal arrives (with a frequency of 1 Hz) at the trigger board, which determines the time shift between the PPS signal and the trigger signal from EAS events within accuracy of 100 ns.

(ii) Electronic compass with a resolution of  $0.5^\circ$  for determining the azimuthal angle of the setup position. Since the setup position in the horizontal plane is not fixed and depends on the wind direction, the information from this sensor allows one to reconstruct the



Fig. 13. Installation of the SPHERE-2 setup on the Lake Baikal ice.

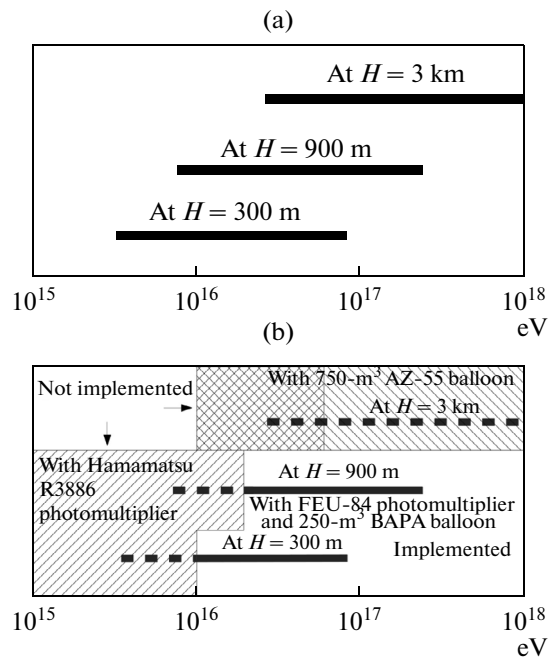


**Fig. 14.** (a) Initially planned measurements of the spectrum in different energy ranges at altitudes  $H$ ; (b) Actually carried out measurements.

setup position with respect to the Earth and analyze anisotropy of the cosmic-ray arrival.

(iii) Inclinometer for determining the setup tilts with respect to the horizontal plane within accuracy of  $0.25^\circ$ . The measurements are carried out in two vertical (mutually perpendicular) planes. Deviations arise when the wind load on the setup case changes.

(iv) Sensors for measuring the environmental temperature and the temperature in the electronics container. Using data of the temperature sensors, the on-board computer can maintain the optimal electronics-container temperature by controlling the cooling system.

(v) Sensors for measuring the setup pressure and the snow-surface level pressure (with an error of 100 Pa in the range of 750–1100 hPa).

Data of the temperature and pressure sensors mounted on the system and observation surface make it possible to monitor a change in the atmospheric density near the Earth (400–700 m above the surface). For example, during the expedition of 2013, the atmospheric density was found to change by 3% ( $\sim 30$  g/cm<sup>3</sup>) over 2 days. At the same time, the measurements carried out at the ground revealed no significant changes. If the atmosphere is not monitored near ground-based systems, such density fluctuations may lead to a systematic error in determining the depth of cascade-development maximum in atmosphere.

#### 4.3. Series of Measurements on the SPHERE-2 Setup

Initially, it was planned to carry out series of measurements on the SPHERE-2 setup in a wide energy range at different altitudes (Fig. 14a). However, expected Hamamatsu R3886 photomultipliers were replaced with less expensive FEU-83-3 due to underfunding of the experiment. Since FEU-83-3 photomultipliers are characterized by lower sensitivity (by a factor of 3) and smaller sensitive photocathode area (by a factor of 2) as compared with Hamamatsu R3886, the signal-to-noise ratio was lower than the expected value by a factor of 2.5. This increased the energy threshold to  $10^{16}$  eV. In addition, the underfunding made purchasing helium impossible, and thus it was decided to do without a 750-m<sup>3</sup> AZ-55 balloon, which can lift the setup to an altitude up to 3 km. These factors deteriorated the quality and quantity of the experimental data. Figure 14b shows the implemented part of the initial plan.

The chosen place for releasing a balloon with the SPHERE-2 setup was near the 107th km of the Krugobaikalskaya railway at the Baikal Neutrino Station of the Institute for Nuclear Research, Russian Academy of Sciences, at a distance of 1 km from the coast line. The SPHERE-2 setup was launched for the first time from the Lake Baikal ice in March of 2008. The purpose of the expedition was to try out balloon releases under real climatic conditions and interaction with the Aeronautical Service of Irkutsk Region, and to check operating capacities of the setup and ground-

**Table 2.** Sequence of LED switching (clock-period duration 375 ns; x indicates switching on LED and an empty cell indicates switching off LED)

LED	Clock period														
	1	2	3	4	5	6	7	8	9	10	11	12	13	14	15
7	x	x							x						
6	x	x	x							x					
5	x	x	x	x							x				
4	x	x	x	x								x			
3	x	x	x	x	x								x		
2	x	x	x	x	x	x								x	
1	x	x	x	x	x	x									x

**Table 3.** Overall result of the expeditions with the SPHERE-2 setup

Year	Total time (h:min)	Trigger signals in total	Found events from EAS	Number of photomultipliers in the array
2008	1:30	—	1	20
2009	11:00	—	0	64
2010	29:10	1343	36	95
2011	33:03	20542	220	95
2012	31:12	7716	364	109
2013	33:17	3813	459	109
2008–2013	139:12	33414	1080	—

based equipment. The SPHERE-2 setup was lifted using a specially designed and fabricated 250-m<sup>3</sup> Baikal captive balloon (BAPA) to an altitude of about 710 m above the Lake Baikal level. The system stayed at this altitude for about three hours and 1.5 h in the EAS detection mode. Afterwards, the altitude of detector position above the snow surface (400–900 m) was set according to the wind conditions.

The compilation of data obtained in the measurements is given in Table 3. A small number (in comparison to the ground-based experiments) of events in this experiment is due to a high energy threshold for observing reflected EAS CL. To increase the detection efficiency, the setup was modified for the next five years. In 2009, no events from EAS were detected because of a malfunction in the high-voltage power supply for photomultipliers. In 2010, the SPHERE-2 setup was lifted seven times. EAS CL was measured during six launches. The parameters were reconstructed for 36 EAS events. In 2011, the introduction of integrating discriminators made it possible to reduce the detection threshold and increase the efficiency by a factor of about 6. By 2012, the step of digitizing photomultiplier anode signals was reduced to 12.5 ns and the sensitivity of preamplifiers at the inputs of measuring channels was increased by a factor of 3. Thus, the detection efficiency was further increased by a factor of  $\sim 1.5$ . The maximum efficiency (exceeding the initial one by a factor of 11) was achieved in 2013 after mounting a new seven-segment mirror with a better reflectance.

#### 4.4. Estimation of the Detection Accuracy and Detector Calibration

It was shown in the Introduction that the technique for detecting reflected EAS CL provides high measurement accuracy. In turn, the electronics and photomultipliers of the detector should ensure a comparable or better accuracy of detecting and digitizing light pulses arriving at photomultiplier photocathodes. A series of laboratory test measurements was carried out in order to determine the accuracy of the measuring equipment.

**4.4.1. Consideration of distortions in signal digitization.** To check the accuracy of signal digitization and reveal distortions introduced by photomultiplier distributed capacitances and operational amplifiers, the pulses digitized by the measuring board of the system with a step of 12.5 ns were compared with the corresponding oscillograms recorded by a LeCroy WaveJet 322 oscilloscope [80] with a step of 0.5 ns. The measurements were carried out as follows. Two photomultipliers, FEU-84-3 and Hamamatsu R3886 (served as a reference photomultiplier), observe a horizontally oriented screened scintillator unit from opposite sides. The particles passing through the scintillator yield short (pulse duration  $\sim 5$  ns) intense flashes recorded by both photomultipliers. The signal from each photomultiplier is split and fed to two channels of the measuring board of the system and two oscilloscope channels. The produced charges are estimated based on two oscillograms and compared.

Figure 15 shows the relationship between the charge values reconstructed based on the data of the measuring channel of the SPHERE-2 setup and

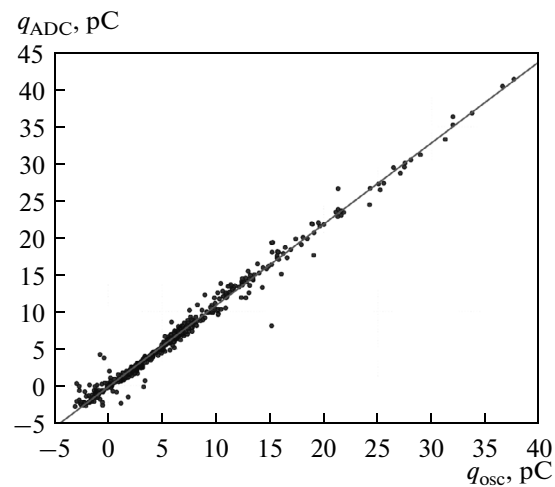


**Fig. 15.** Comparison of the results of measuring the anode signal charge of FEU-84-3 photomultiplier reconstructed based on data of the measuring channel of the SPHERE-2 setup and data from a LeCroy WaveJet 322 oscilloscope.

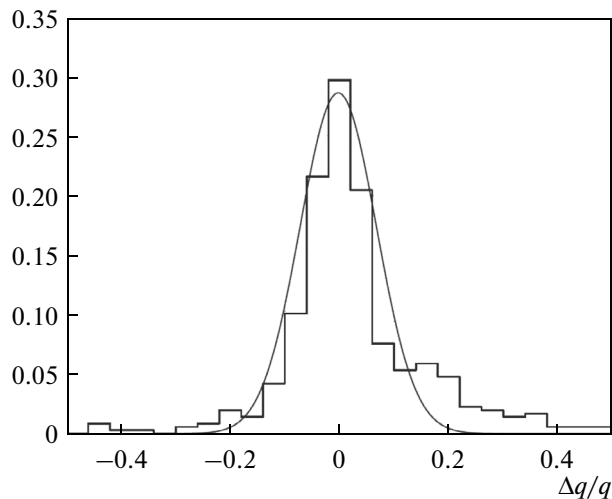


**Fig. 16.** Histogram of the relative error in determining the charge and its approximation by a Gaussian distribution with  $\sigma = 0.06$ .

the oscilloscope data. Figure 16 shows the histogram of the relative error in determining the produced charge on the assumption of exact reconstruction of the charge based on the oscilloscope readings. It can be seen that even at low digitization frequency the error in reconstructing charge by the setup equipment is  $\sim 6\%$  for the shortest pulses. Such a small error is due to a low time resolution of FEU-84-3 and integration of the signal by operational amplifiers at the inputs of the measuring channels. In this case, the pulse waveform is distorted but the charge value is retained. I.e.,

even short signals can be effectively integrated. An analysis of Figs. 15 and 16 suggests that pulses with the smallest amplitude are reconstructed with the lowest accuracy. For large amplitude pulses, the error in reconstructing the produced charge is 3–4%. When measuring EAS CL, a typical pulse has a width of 100–150 ns due to the geometry of the field of view of an individual photomultiplier, which reduces the error in digitizing such pulses to 1–2%.

**4.4.2. Consideration of photomultiplier nonlinearity.** To reduce the influence of a high background-illumination level when carrying out the measurements, the photomultiplier gains were reduced by connecting the last dynodes to the anode. This led to nonlinear sensitivity characteristics. The photomultiplier nonlinearity is controlled based on data of the LED calibration system, which was described in Section 4.2.2. Since the calibration frame contains both single LED flashes and various combinations of simultaneous switching (see Table 2), the sum of single-signal intensities can be compared with the intensity of simultaneous switching. In the case of linear photomultiplier response, the measured intensity of simultaneous diode switching and the sum of individual-diode intensities are expected to be equal. Figure 17a shows the results of measuring linearity for 108 FEU-84-3 photomultipliers and one Hamamatsu R3886 photomultiplier. In comparison with FEU-84-3, Hamamatsu R3886 has a worse characteristic because of the design of dynode system and necessity of connecting more dynodes to reduce the gain to the level of FEU-84-3. The mechanisms of occurrence of photomultiplier nonlinearity and the procedures of its cor-

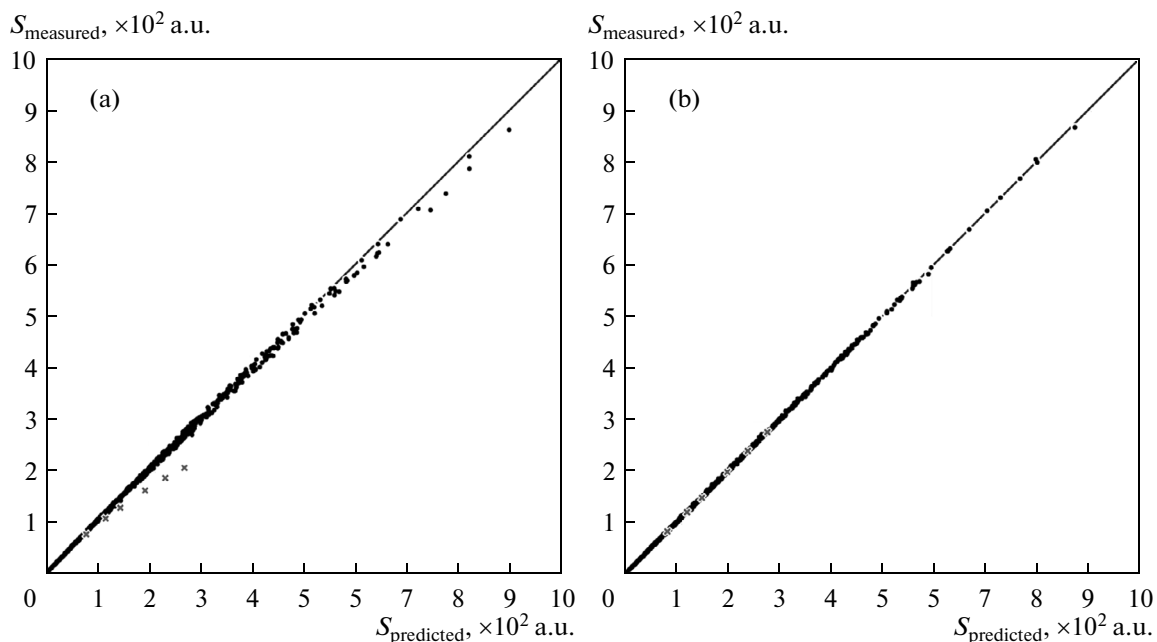


**Fig. 17.** Measured characteristics of linearity for 109 photomultipliers in the photodetector array (a) before introducing corrections and (b) after it: (dots) all FEU-84-3 photomultipliers and (crosses) Hamamatsu R3886 photomultipliers.

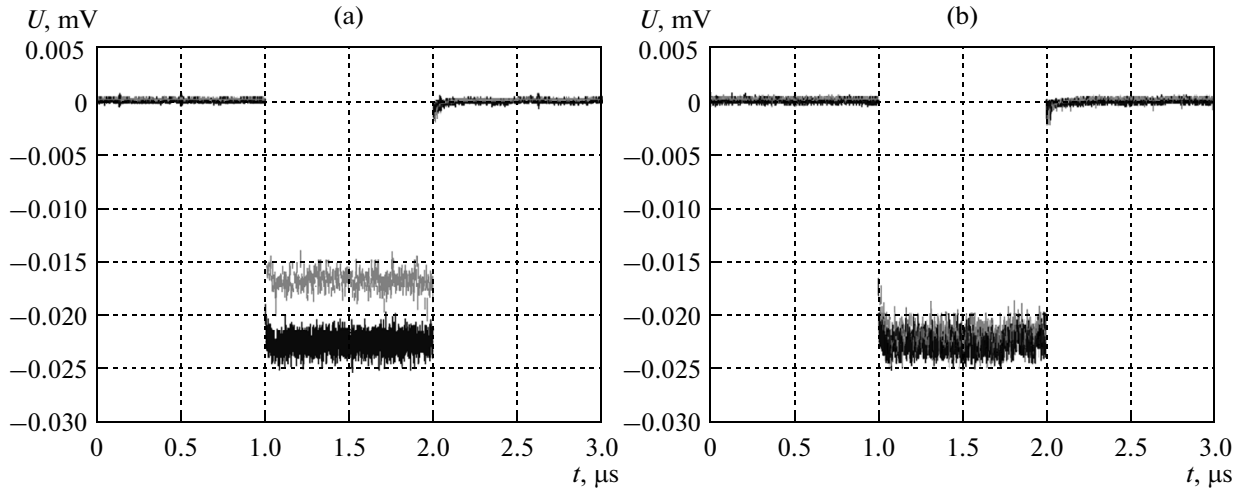


**Fig. 18.** Pulse amplitudes recorded by (gray line) FEU-84-3 and (black line) Hamamatsu R3886 photomultipliers: (a) in darkness and (b) under illumination (signals almost coincide).

rection were described well in [81]. After introducing the necessary corrections (Fig. 17b), the dependence of the number of photons at the photocathode on the amplitude at the anode becomes close to linear. The above-described procedure is carried out independently for each measurement session based on data of the calibration frames.

**4.4.3. Relative calibration.** The initial selection of FEU-84-3 implied verification (for all photomultipliers) of the sensitivity and operation stability in darkness and under illumination equivalent to the stellar-sky background, which provides the anode current of 5–10  $\mu\text{A}$ . Hamamatsu R3886, the characteristics of which weakly depend on the illumination, was chosen as a reference photomultiplier. Responses of each photomultiplier to a rectangular light pulse were studied and compared with responses of the reference photomultiplier. Figure 18 shows examples of pulses for one FEU-84-3 photomultiplier in the absence and presence of illumination. It can be seen that the sensitivity of Hamamatsu R3886 barely changes, whereas the sensitivity of FEU-84-3 under illumination increases by a factor of  $\sim 1.3$ .

The light-background value fluctuates during the experiment because of a change in weather conditions; therefore, the sensitivity of all detector photomultipliers has to be monitored systematically. To perform flight calibrations, the reference Hamamatsu R3886 photomultiplier was placed at the center of the photomultiplier array. Photomultipliers are calibrated with respect to the reference one based on data of the LED calibration systems described in Section 4.2.2. Each photomultiplier records a flash from calibration LEDs with a known intensity distribution 6  $\mu\text{s}$  after detecting an event from the trigger. The intensity of this pulse is normalized to the pulse intensity in the stable reference Hamamatsu photomultiplier; the

normalized pulse amplitude depends on only the variation in the photomultiplier sensitivity.

The relative sensitivity coefficients are determined on the basis of data of the calibration frame by selecting the mean signal amplitude  $S_j^i$  at each LED switching ( $i$  is the photomultiplier number and  $j$  is the LED number). According to Table 2, the last seven diode switches concern single diodes. For each of these pulses, the intensity  $S_j^1$  in the first reference photomultiplier is determined.

Taking into account the relative arrangement of photomultipliers and diodes, angular distribution of diode radiation, coefficient of reflection from a photomultiplier glass, and the dependence of the latter on the angle of incidence of photons, the responses  $A_j^i$  of each photomultiplier in the array with a number  $i$  to a pulse from a LED with a number  $j$  were calculated. On the assumption that the measured pulse intensities  $S_j^1$  from each diode in the first photomultiplier are true flash intensities, the theoretical signal in each photomultiplier is calculated (taking into account responses  $A_j^i$ ) as  $T_j^i = A_j^i S_j^1$ . Then the signal from a flash of several diodes is calculated for each photomultiplier and the total expected signal from a sum of all flashes of the same diodes is calculated. Afterwards, the calibration coefficients  $K^i$  are calculated as a ratio of the total expected signal to the measured one.

Thus, the sensitivities of all photomultipliers are reduced to that of the Hamamatsu R3886 photomultiplier, the characteristics of which weakly depend on time and illumination (in contrast to less stable FEU-84-3) (see Fig. 18). This procedure is carried out for each event.

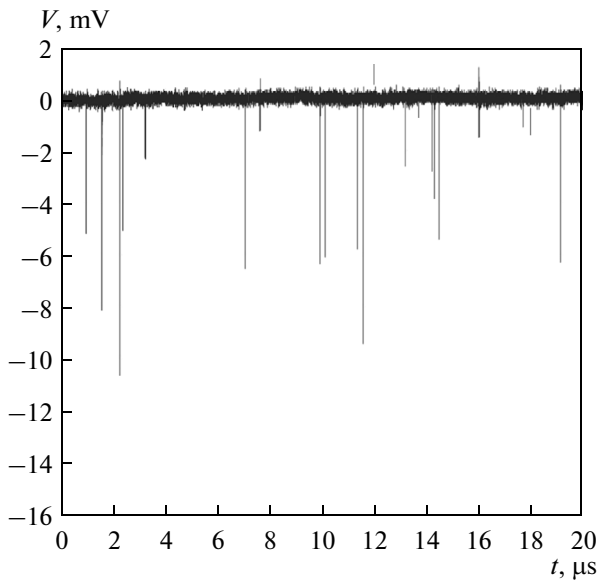


**Fig. 19.** Fragment of the oscillogram of charge pulses from the anode of a Hamamatsu R1924A-100 photomultiplier illuminated by a Hamamatsu L11494-430 calibration source.

**4.4.4. Absolute calibration.** It was shown in Section 4.4.3 that the relative calibration of all photomultipliers in the array is reduced to the sensitivity of the Hamamatsu R3886 photomultiplier. Therefore, the absolute photomultiplier calibration can be found by determining under laboratory conditions the parameters and absolute sensitivity of the latter photomultiplier.

A Hamamatsu L11494-430 device with a light-flux power of 1.002 pW ( $\sim 2.12 \times 10^6$  photons per second) was used as a reference light source. This source has a diffuse-radiation region 7 mm in diameter and is characterized by a peak emission wavelength of 430 nm, emission band FWHM of 65 nm, and radiation stability of  $\pm 2\%$ .

The absolute calibration cannot be performed using an existing light source in the current version of Hamamatsu R3886 arrangement in the array due to intrinsic sensitivity and gain. An interim Hamamatsu R1924A-100 photomultiplier, which is characterized by the photocathode quantum efficiency of 35% and the dynode-system gain up to  $2 \times 10^6$ , was calibrated. This photomultiplier was brought into contact with the light source and taken off into the mode with a maximum gain (i.e., photoelectron counting mode).

Figure 19 shows a fragment of the oscillogram of the signal obtained. The pulses from single photoelectrons can be clearly seen against the low noise background. The distribution of charges in pulses from photoelectrons is shown in Fig. 20. The peak from single photoelectrons is pronounced. One photoelectron yields a charge of  $\sim 0.5$  pC on average. This distribution also indicates that the total number of

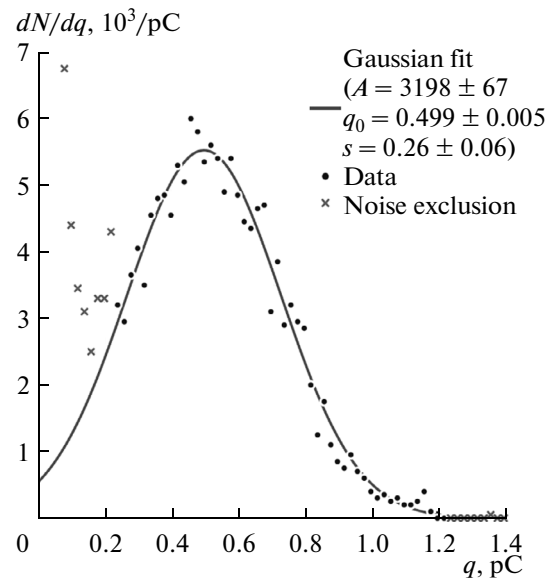


**Fig. 20.** Distribution of the charge from one photoelectron collected at the anode. The solid curve indicates the approximation by the Gaussian function.

photoelectrons recorded for 4 ms is  $3197 \pm 67$  photoelectrons. Hence, taking into account that the expected number of photons from the light source for this time interval is  $8480 \pm 150$ , the quantum efficiency of the Hamamatsu R1924A-100 photomultiplier is  $37.7 \pm 1.1\%$ .

To relate the R3886 sensitivity to the measured R1924A-100 sensitivity, the following procedure was performed. Both photomultipliers were placed close to each other at a distance of 40 cm from a FYL-5013 VC1C light source (see Section 4.2.2). An opaque scatterer equalized illuminance at both photomultipliers. Diaphragms 6 mm in diameter were mounted on the photocathodes of both photomultipliers to equalize light fluxes. R1924A-100 photomultiplier operated in the same mode as in the measurement with the Hamamatsu L11494-430 light source. R3886 photomultiplier was put into the maximum-amplification mode. The signals from both photomultipliers from the same light pulses of the light source were measured. It was found that the charges of 87.43 and 6.10 nC drained from the R1924A-100 and R3886 anodes, respectively, for 30  $\mu$ s. Three series of these measurements were carried out. One photoelectron yields a charge of 0.499 pC on the R1924A-100 anode on average; therefore, with allowance for the quantum efficiency, the light flux in R1924A-100 was  $(465 \pm 14) \times 10^3$  photons. On the assumption of equal light fluxes at both photomultipliers, it was found that the mean sensitivity of the R3886 photomultiplier is  $75.9 \pm 2.3$  photon/pC in the maximum-amplification mode.

When measuring EAS CL, the R3886 gain was several times smaller than that found in the calibration

measurement. Therefore, the sensitivity was determined for real expedition conditions by considering the background illumination. For example, the measurement conditions of 2013 gave the mean estimate of the R3886 photomultiplier sensitivity to be 6.5 photons per code unit.

The error in absolute calibration is no more than 3% for the R3886 photomultiplier and about 5% for any photomultiplier in the array if the relative calibration uncertainty is taken into account.

## 5. SIMULATION AND DATA ANALYSIS

As was noted above (see Section 3), the main purposes of processing data of the SPHERE experiment are as follows:

(i) Reconstruction of the spectrum of all PCR nuclei with a detailed investigation of its systematic and methodical errors:

(1) calculation of the fiducial acceptance of detecting showers;

(2) estimation of the energy of primary particles of showers detected in the experiment.

(ii) Separation of PCR elemental groups:

(1) estimation of the SDF slope for the detected EASs;

(2) consideration of the dependence of the fiducial acceptance on the nuclear mass.

In this study, EAS CL SDF slope index  $\eta$  (equal to the ratio of the number of Cherenkov photons in a circle centered at the shower axis to that in some ring) served as a parameter sensitive to the PCR composition.

### 5.1. Model of Detector Response

The algorithm of simulating detector response consists of three successive procedures:

(i) Calculation of the spatial and temporal structure of EAS CL for a sample of showers.

(ii) Simulation of the optical-system and photomultiplier responses.

(iii) Consideration of the electronics response.

**5.1.1. Model of the spatial and temporal structure of EAS CL.** The spatial and temporal structure of EAS CL was calculated using the CORSIKA 6.500 package [82] with two versions of the model of nucleus–nucleus interaction at high energies: QGSJET-I-01c [83–85] and QGSJET-II-03 [86, 87] (referred to as, respectively, QGSJET-I and QGSJET-II below); the model Gheisha-2002d was used for low energies [88]. The observation surface (on the Lake Baikal ice) is at an altitude  $H_{\text{obs}} = 455$  m above the sea level. The simulation was carried out taking into account the spectral dependence of the quantum efficiency of FEU-84-3 photomultipliers used in the SPHERE experiment. The primary-particle energies  $E_0$  were 1, 3, 5, 10, 30, and 100 PeV; the calculation was performed for pri-

mary nuclei of four types (protons and helium, nitrogen, and iron nuclei) in three ranges of zenith angles:  $0^\circ$ – $20^\circ$ ,  $20^\circ$ – $40^\circ$ , and  $40^\circ$ – $60^\circ$ . The shower arrival directions are isotropically distributed in each range. The distribution over the azimuthal angle is uniform in all cases.

The simulation result for one shower was a three-dimensional array of the number of Cherenkov photons arriving at the observation surface consisting of  $480 \times 480$  spatial bins (each  $2.5 \times 2.5$  m in size) and 102 time bins (each of 5 ns). Time at each surface point is counted from the instant of arrival of the plane front related to the leading particle.

A complete statistical simulation yielded a sample of the spatial and temporal distributions of EAS CL for about 2000 showers with different parameters. This provided the most comprehensive consideration of the fluctuations in EAS development, which is extremely important for the problem of studying the nuclear composition of PCRs with superhigh energies.

**5.1.2. Simulation of the optical-system and photomultiplier responses.** The next stage of calculating the detector response is consideration of the geometric and optical effects introduced by the SPHERE-2 setup, which distort the signal observed. The calculation input data are EAS CL histograms formed at the previous step.

To analyze the experimental data of 2010–2011, a somewhat simplified version of the response model was developed [52, 89]. The partial photon reflection from the photomultiplier glass and the polarization effects were disregarded in this version. The optical-system response was simulated using the method based on tracing a large number of rays with different initial parameters [90]. Some details of this procedure were reported in [89]. An improved version of the detector response model developed for analyzing the data of 2012–2013 [55, 91] was implemented in the standard Geant4 environment [92]. The spectra of all PCR nuclei obtained for 2010–2011 and 2012–2013 and reconstructed using different model versions are in good agreement.

The calculation result for one shower is an array of photoelectrons, each of which is characterized by the photocathode number of the photomultiplier where this photoelectron is formed and its formation time. The photon-arrival delay  $\tau$  caused by an additional distance, which photons pass from the snow surface to the detector, is taken into account:

$$\tau = (x \cos(\phi_0) \sin(\theta_0) + y \sin(\phi_0) \sin(\theta_0) + \sqrt{H^2 + x^2 + y^2})/c, \quad (2)$$

where  $(x, y)$  are the coordinates of the point on the observation surface, of which the photon is emitted;  $H$  is the altitude of detector position above the observation surface; and  $(\theta_0, \phi_0)$  are the primary-nucleus direction angles. Each of 109 photomultipliers of the

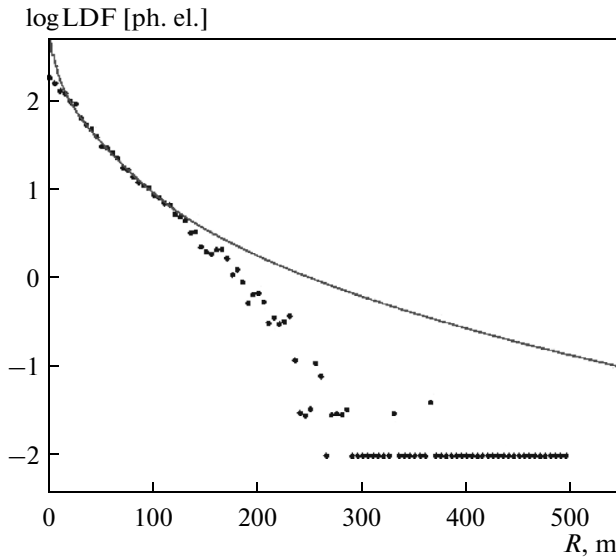


**Fig. 21.** (circles) Example of the “combined model SDF” for a proton with the energy of 10 PeV and the observation altitude of 400 m and (curve) the initial SDF.

SPHERE-2 detector observes a certain area, which leads to an additional (in comparison with the previous calculation step) pulse broadening.

About 500000 detector responses were calculated for the analysis carried out in this study using  $\sim 10^3$  model showers with the primary-nucleus energy of  $10^{16}$ ,  $3 \times 10^{16}$ , and  $10^{17}$  eV within the QGSJET-I model. The simulation was performed for several altitudes of detector position above the observation surface in the range of 400–900 m, and each model shower was used 100 times with different random axis positions uniformly distributed in a square with the length of the side of  $1.5H$ . Since the diameter of the field of view is proportional to the altitude  $H$ , this choice of the axis distribution field made it possible to simulate not only showers with axes in the field of view of the system but also “external” showers.

**5.1.3. Simulation of the electronics response.** The influence of the photomultiplier time characteristic and digitization effects on the recorded signal was taken into account in the last stage of calculating the detector response. As was noted above (see Section 4), the number of photoelectrons per code unit for observation season 2010–2011 was larger than that for 2012–2013 by a factor of 3; digitization was performed with a step of 25 ns in 2010–2011 and 12.5 ns in 2012–2013. However, the technique of calculating the detector response allowed one to use the same photoelectron arrays formed at the previous calculation step in both cases.

Model SDFs were used in this study to estimate the primary-nucleus energy (see Section 5.5). The first simulation results showed that fluctuations in the detector response for the distances from the shower

axis of more than 100 m are rather large at energies on the order of  $10^{16}$  eV. It was decided to use in the energy-estimation procedure average SDFs rather than individual ones; each average SDF was obtained using 100 model responses calculated for the same model shower. During averaging SDF, the geometric and optical effects, distorting the signal values in comparison with the densities of EAS CL in the detector fields of view, were compensated for.

Figure 21 shows (circles) an example of the average model SDF obtained (values in photoelectrons, averaging over distance segments of 5 m) and (solid curve) the initial model shower summed over time. To make the representation on semilogarithmic scale more convenient, a value of 0.01 photoelectrons is added to the average SDF. The initial SDF curve obtained with the geometric and optical effects neglected is normalized to coincide with the average model SDF at distances from the shower axis of about 50 m. Fluctuations in the average SDF are small even at distances of more than 100 m. As one would expect, the initial and average SDFs are in good agreement in the distance range of 30–130 m. At 30 m, the intensity of the average SDF is lower than that of the initial one as a result of different geometric and optical effects: averaging over extended fields of view and action of the mirror spherical aberration. At relatively large distances (above 130 m), a decrease in the values of the average SDF can be explained by the effect of signal digitization by the detector electronics: the values that are smaller than 0.5 code unit in each time bin are measured as zero code unit.

## 5.2. Calculation of the Fiducial Acceptance

The simulation of the fiducial acceptance of detecting showers has been realized by considering the observation conditions varying during the flight. The result of this calculation is especially sensitive to a large change in the altitude of detector position above the snow surface and variations in the response thresholds of the detector measuring channels. The algorithm of calculating the acceptance consists of three steps:

(i) Simulation of the trigger response of the SPHERE-2 setup.

(ii) Calculation of the dependence of the acceptance  $S(E_0, Z, H)$  on the primary-nucleus energy  $E_0$  for different nucleus charge numbers  $Z$  and detector-position altitudes  $H$ .

(iii) Interpolation of the acceptance to some other altitudes in the range of 400–900 m.

**5.2.1. Simulation of the trigger response.** To date, no experiment found a significant deviation from isotropy in the energy range of 10–500 PeV [22, 49, 93], in which the overwhelming majority of showers recorded by the SPHERE-2 detector occur. Since the number of events from EAS CL detected in the SPHERE experiment is small as compared to large

experiments, the acceptance was calculated on the assumption of isotropic arrival directions of PCR nuclei.

Let us introduce the parameter  $A4$  (a sum of four successive values in one measuring channel, which are separated in time by 25 ns). This condition is the same for observation seasons 2010–2011 and 2012–2013. The trigger condition for the SPHERE-2 detector was a combination of two conditions: the parameter  $A4$  should exceed the trigger response threshold in a time window of 1  $\mu$ s in three adjacent channels forming a small equilateral triangle in the photomultiplier array (“local” trigger  $L3$ ), or the parameter  $A4$  should satisfy the same condition in five arbitrary channels (“global” trigger  $G5$ ). In this study, the trigger response was simulated for a “hybrid” condition  $L3/G5$  using the base of detector responses precalculated separately for each flight and each of the angle ranges  $0^\circ$ – $20^\circ$  and  $20^\circ$ – $40^\circ$  [55, 91].

The channel response thresholds were recorded and monitored during the whole observation time. A threshold value in each channel (as well as intensities in the model responses) is expressed in code units; however, it includes the instrumental pedestal level. The pedestal level was determined in the preliminary processing of the experimental data and subtracted from the threshold value. In addition, it was taken into account during the simulation that the sensitivities of real-detector channels differ and are characterized by the relative calibration coefficients (see Section 4.4.3). The entire simulation procedure was performed for an “average” (typical) measuring channel. Before the procedure of simulating the trigger response, the measured thresholds are multiplied by the values of the corresponding calibration coefficients.

Finally, we should note that the energies of model showers are discrete and equal to  $10^{16}$ ,  $3 \times 10^{16}$ , and  $10^{17}$  eV. To estimate the acceptance at intermediate energies  $E$  of the model-event intensity, the corresponding energies  $E_0$  were multiplied by the coefficient  $E/E_0$  (the minimum and maximum “effective energies”  $E$  were about  $2 \times 10^{15}$  and  $10^{18}$  eV, respectively). This can be done because (as will be shown below) the acceptance barely changes at energies above  $10^{17}$  eV. A systematic error caused by this calculation procedure will also be considered below.

**5.2.2. Calculation of the acceptance for discrete values of the altitude.** To reconstruct the spectrum of all PCR nuclei, a reference area was chosen in the form of a circle with a radius equal to the radius of the detector field of view plus 100 m. The zenith-angle range was chosen to be  $0^\circ$ – $40^\circ$ . This choice is caused by the necessity of including the maximum possible number of events into the analysis (together with some “external” events with axes beyond the detector field of view). At the same time, the error in estimating the energy of showers with axes spaced by more than 100 m from the edge of the field of view sharply

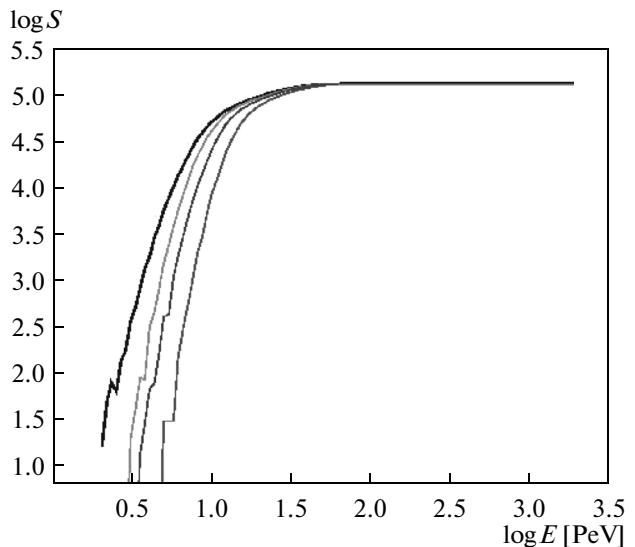


**Fig. 22.** Result of calculating the acceptance for the zenith-angle range of  $0^\circ$ – $20^\circ$ , observation altitude of 500 m, thresholds of the third flight of observation season 2013, and primary nuclei of different types: protons and helium, nitrogen, and iron nuclei ( $Z = 1, 2, 7,$  and  $26,$  respectively, in ascending order with respect to the threshold) [55].

increases (see Section 5.5); in this context, it was decided to exclude these events from the procedure of reconstructing the spectrum.

Some examples of the dependences of the fiducial acceptance  $S$  on energy are shown in Fig. 22 for different nuclei. It can be seen that below some energy (in this case, below  $(1.5$ – $2.0) \times 10^{16}$  eV) the parameter  $S$  sharply decreases with a decrease in energy and begins to depend strongly on the primary-nucleus charge. This circumstance is one of the main difficulties hindering the reconstruction of the spectrum of all PCR nuclei in the SPHERE experiment.

The calculation results similar to those shown in Fig. 21 were obtained for only several altitudes  $H$  (400, 500, 580, 700, and 900 m), at which the SPHERE-2 setup stayed for the major observation time. The altitudes of detector position for events caused by EAS CL are plotted in Fig. 23 for observation season 2013. The acceptance values at intermediate altitudes were determined by interpolation. An example of the interpolated dependence  $S(H, \log(E))$  is shown in Fig. 24 for the case of primary protons and the zenith-angle range of  $0^\circ$ – $20^\circ$ .

### 5.3. Estimation of the Accuracy of Calculating the Acceptance

The accuracy of estimating the acceptance is affected by several factors. The error in measuring the altitude of the detector is small; its influence is mainly reduced to a small change in the normalization of the acceptance curve corresponding to a specified alti-

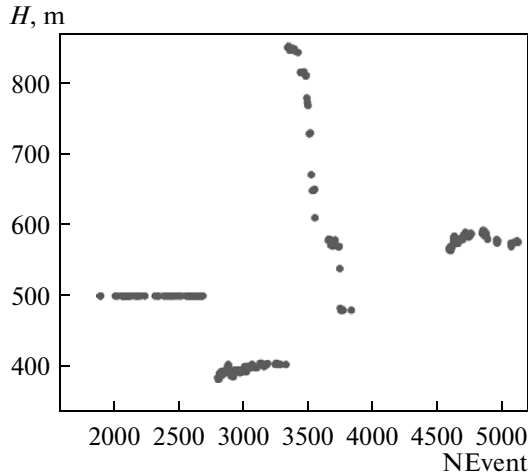


**Fig. 23.** Altitudes for EAS CL events detected during observation season 2013.

tude. Uncertainties in estimating the thresholds, which are determined by the accuracy of reconstructing the instrumental pedestals of no more than 0.5 code units and the relative calibration coefficients (below 3%), also weakly affect the calculation results. The error due to these factors is about 1%. Under these conditions, the acceptance is mainly affected by the mean discriminator threshold, whereas the shape of distribution around this value is much less important.

Some systematic uncertainty in estimating the acceptance arises as a result of the use of discrete energies of model events and interpolation of the acceptance to intermediate altitudes of the observation. However, the results of comparing the acceptances, calculated using the model responses with different primary-nucleus energies and observation altitudes, showed that this error is about 1–2% at energies above  $10^{16}$  eV. A small value of the above-described effect can primarily be explained by a slow change in the shower development behavior with a change in the primary-nucleus energy.

At relatively low energies ( $E_0 < 10^{16}$  eV), this error may increase (especially for heavy nuclei (nitrogen or iron) and large observation altitudes (above 700 m)) because the signal-digitization effects differ for different primary-nucleus energies and cannot be reduced to a simple multiplication by a constant. As demonstrated above (Fig. 21), the digitization effects are important in the range of distances from the axis where the SDF values are below 3 photoelectrons. However, most threshold values (in photoelectrons) exceed 3 photoelectrons. In addition, the energies, at which the digitization effect begins to affect the fulfillment of the trigger condition for SDFs similar to that shown in Fig. 21, are below  $3 \times 10^{15}$  eV. Thus, the influence of the above-described effect on the results of calculating the acceptance is small.

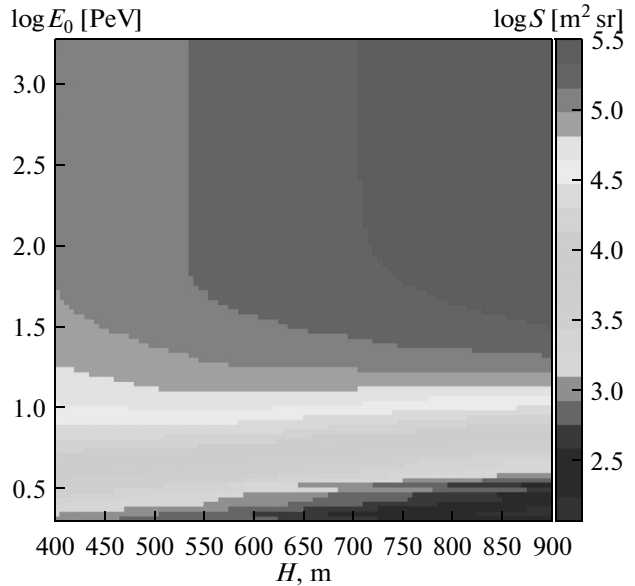


**Fig. 24.** Acceptance as a function of the altitude and primary energy ( $p$ ,  $0^\circ$ – $20^\circ$ ).

A statistical uncertainty in calculating the acceptance due to a finite number of the used events is relatively small (no higher than 2%) at energies above  $10^{16}$  eV.

#### 5.4. Reconstruction of SDF of Experimental Events

The primary-nucleus energy is estimated based on SDF of experimental events. SDF was reconstructed by integrating the detected signal over time. An example of the initial event after subtracting backgrounds is shown in Fig. 25a. One can see oscillograms for 109 measuring channels. The channel numbers and relative time are plotted on the horizontal and vertical axes, respectively. Each bin corresponds to one ADC measurement. The color strength in the rectangle is proportional to the pulse amplitude (black color indicates the maximum amplitude in the event).

It can be seen in the figure that, within this representation of oscillograms, time intervals with maximum pulse amplitudes in the measuring channels form a curve with a complex sinusoidal shape. This pattern is due to a mutual position of the channels in the photodetector array shown in Fig. 25b. Photocathodes of the photomultipliers in the array are arranged so as to make a hexagonal structure and circularly enumerated from the center so that the central photomultiplier number is 1, the first ring consists of photomultiplier with numbers 2–7, and so on. Each subsequent period of the curve in Fig. 25a corresponds to the measuring channels of photomultipliers forming a larger ring on the array surface.

The first step of the procedure of reconstructing SDF is a search for the shower front. The time bins in

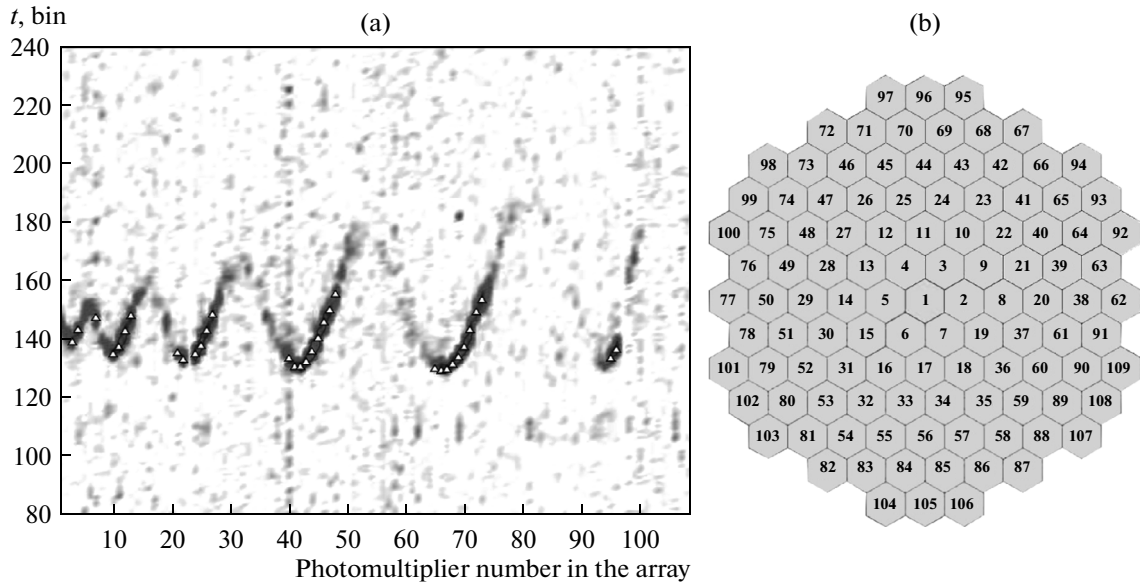


**Fig. 25.** (a) Example of the representation of an experimental event. The measuring channel numbers are plotted on the horizontal axis and the relative times with the ADC measurement step of 1 bin = 12.5 ns are plotted on the vertical axis. The color strength in the rectangle corresponds to pulse amplitude (black color indicates the maximum amplitude in the event). (b) Arrangement of the channel numbers in the photomultiplier array.

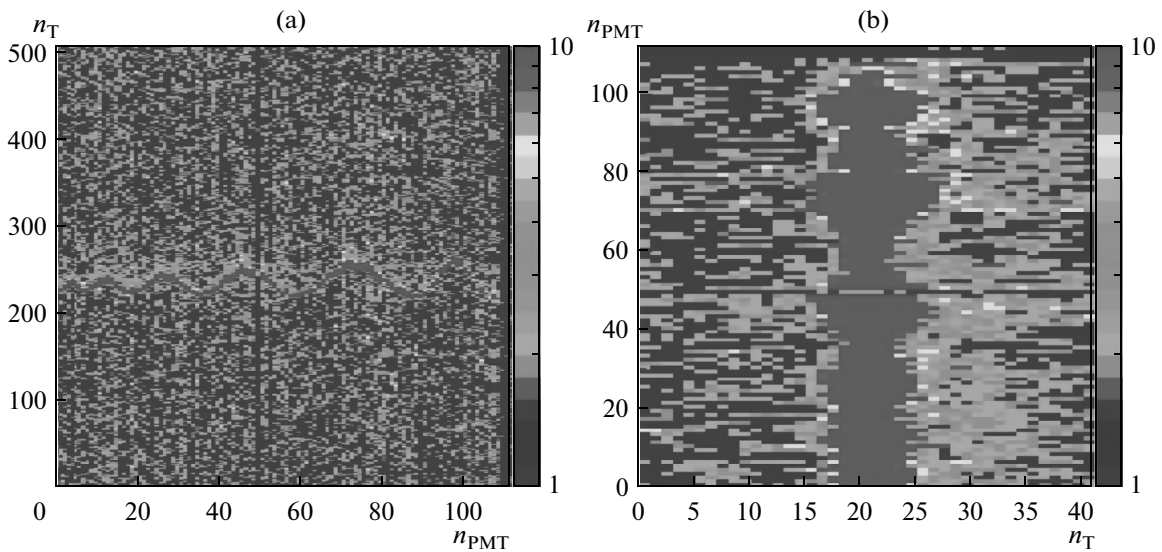


**Fig. 26.** (a) Example of an experimental event recorded during observation season 2013. (b) Fragment of the same event after reconstructing the shower front (here, the event is rotated by 90° and the pulse maximum in all channels is shifted to the region of the 20th time bin).

some channels with a relatively strong signal corresponding to the front are indicated by triangles in Fig. 25a. Another example of the pronounced experimental event with subtracted pedestals is shown in Fig. 26. In this case, bins with a content of more than 10 code units are shown with the same color to demonstrate the shower front more clearly. The front can be searched for by various methods: one of them is described below.

Expression (2) for delay within the plane-front approximation depends on the primary-nucleus direction  $(\theta_0, \phi_0)$ . If the  $(\theta_0, \phi_0)$  values coincide with true ones, the line of the estimated front position passes near the intensity maxima shown in Fig. 26a. After subtracting the delay, the pulse maxima in each channel coincide (Fig. 26b). Having summed the pulses aligned in time (Fig. 26), one can obtain a narrow and high peak. Maximization of the height of this peak

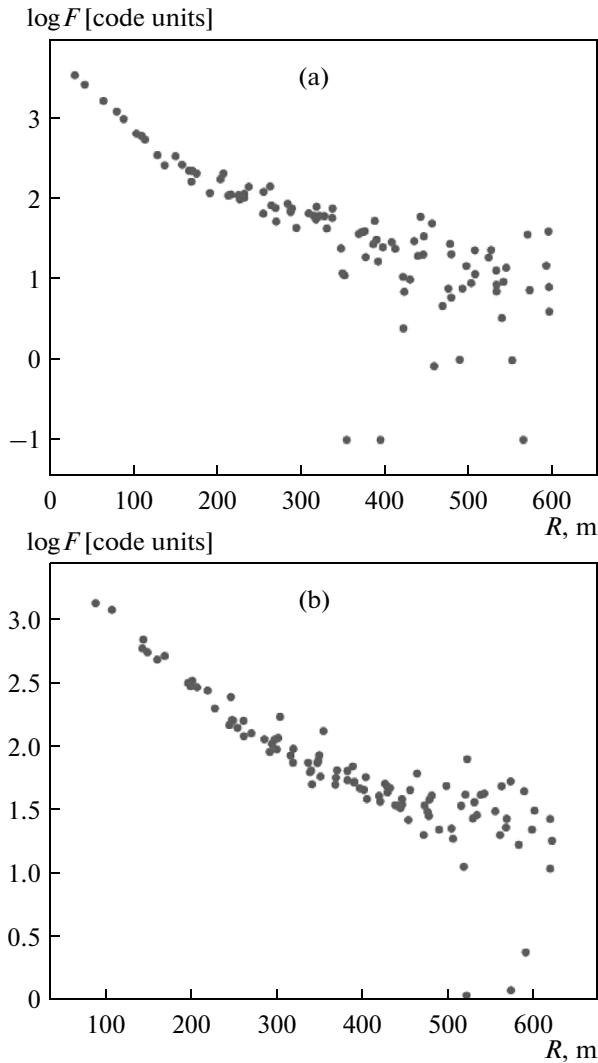


**Fig. 27.** Example of the SDF reconstructed based on data of observation season 2013 for (a) an event with the axis in the field of view of the SPHERE-2 detector and (b) an external event. The signals in channels with zero value are equated to 0.1 code unit.

over the parameters  $(\theta_0, \phi_0)$  yields the pattern shown in Fig. 26b. The integration of pulses over time backward and forward from the maximum, which is in the region of the time bin with number 20 in all channels in Fig. 26b, makes it possible to estimate SDF of the experimental shower.

To represent SDF in a more symmetric form similar to that shown in Fig. 21 for the case of model events, the EAS axis position  $(x_0, y_0)$  must be reconstructed. In model events (in contrast to experimental ones) the axis position is known. The axis coordinates were also estimated using a variational technique through minimization of the functional of quadratic deviation of experimental SDFs from model ones. Two examples of reconstructed SDFs are shown in Fig. 27.

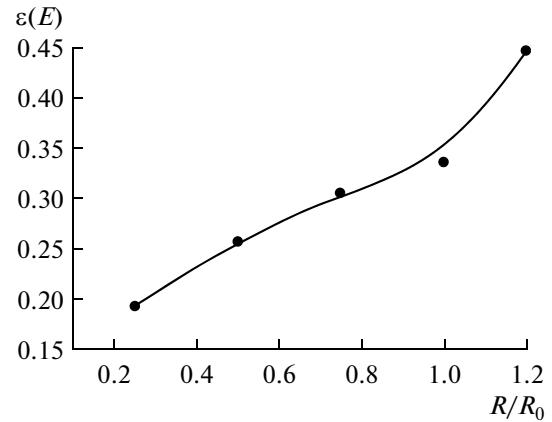


**Fig. 28.** Relative error in estimating the energy as a function of the ratio of the distance between the shower axis and the center of the field of view to the radius of the field of view for the energy of 30 PeV [89].

### 5.5. Estimation of the Primary-Nucleus Energy

Since the fiducial acceptance is calculated without using the information concerning the direction of primary particles of showers detected in the experiment or the coordinates of their axes, the primary-nucleus energy is, strictly speaking, the only EAS parameter necessary for reconstructing the spectrum of all PCR nuclei (if the dependence of the fiducial acceptance on the nuclear composition is neglected). The errors in reconstructing the direction and position of the shower axis induce an additional uncertainty in SDF and affect the result of estimating the energy and, accordingly, the result of reconstructing the spectrum of all nuclei.

To estimate the energy, we used the method where this parameter is measured simultaneously with the reconstruction of the shower axis position by normalizing SDFs of the experimental events to the model SDFs with known energy [94]. The dependence of the relative error in estimating the energy on the ratio of the distance between the shower axis and the center of the field of view to the radius of the field of view estimated from the simulation for the energy of 30 PeV is shown in Fig. 28.

### 5.6. Procedure of Reconstructing the Spectrum of All Nuclei

Based on the model of the acceptance and the estimated energies of the detected events, one can reconstruct the spectrum of all PCR nuclei. To this end, a sample of events detected in 2011–2013 was taken: all “internal” events with the reconstructed coordinates of the shower axis within the field of view and some “external” events, for which the estimated distance from the shower axis to the edge of the field of view did not exceed 100 m. To reconstruct the PCR spectrum, the energy distribution of showers was simulated and

the spectrum shape was chosen so that the model and experimental energy distributions were consistent.

As the first approximation, it is interesting to qualitatively compare the shapes of the experimental-distribution histogram and the model histograms plotted for primary nuclei of different types and the differential PCR energy spectrum with the exponent  $\gamma = -3.0$  for the observation conditions of season 2013 (Fig. 29). The experimental distribution is indicated by circles with statistical errors (circle positions correspond to bin centers). The model distributions have a narrower (with respect to energy) bin and are indicated by curves for primary nuclei of four types: protons and helium, nitrogen, and iron nuclei (in the ascending order in the threshold). At energies below 30 PeV, the model-histogram value depends strongly on the primary-nucleus type (this fact reflects the dependence of the fiducial acceptance on the same parameter (Fig. 21)).

At energies  $E_0 > 50$  PeV, the error in histogram of the experimental energy distribution exceeds the difference in the acceptances between two extreme cases for primary protons and iron nuclei. At these energies, the spectrum of all PCR nuclei for observation season 2013 is adequately described by a power law with the exponent  $\gamma = -3.0$ . At lower energies, additional experimental information (which makes it possible to develop the model of the acceptance for the case of mixed composition not contradictory to the characteristics of recorded events) should be used to reconstruct the spectrum shape.

The dependence of the acceptance on the PCR composition is almost completely determined by the difference in shapes of the SDF for different nuclei at distances from the shower axis of less than 100 m; specifically, intensities in the central part of SDF determine if CL from this shower causes the trigger response (see Section 5.2). In this study, the shape of the SDF central part is described by only the slope index  $\eta$  defined as a ratio of the signal in a circle with a radius of 60 m to the signal in a ring with radii of 60 and 130 m. It was shown that this parameter is fairly sensitive to the PCR mass composition [52]. However, the problem of reconstructing the spectrum of all nuclei does not imply the analysis of the nuclear composition; instead, it would be more correct to speak about an adequate description of the  $\eta$  distribution using a sample of model events. Indeed, the results of reconstructing the PCR mass composition by the aforementioned method depend on the nucleus–nucleus interaction model and some other factors. However, if the model  $\eta$  distribution coincides with the real one, the above systematic uncertainties do not affect the result of measuring the spectrum of all nuclei.

The model acceptance determined using the information about the  $\eta$  distribution is shown by a bold line in Fig. 29. The sample of  $\eta$  values was calculated based

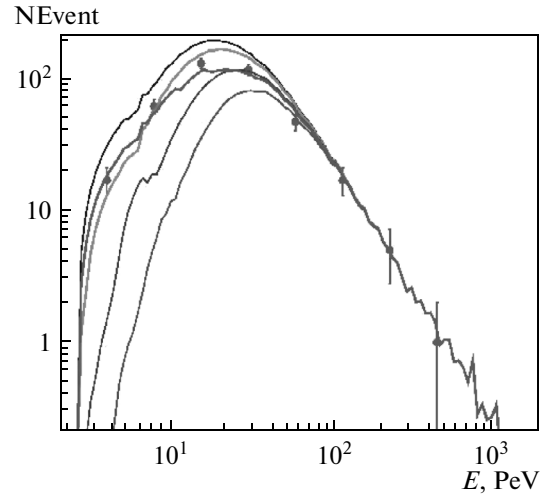


**Fig. 29.** (circles with error bars) Energy distribution of experimental events and (curves) model distributions for primary nuclei of different types: protons, and helium, nitrogen, and iron nuclei (in ascending order with respect to the threshold) for the observation conditions of season 2013. The model distribution for the mixed composition is shown by a bold curve.

on “internal” events and a small number of “external” ones, in which the distance from the reconstructed position of shower axis to the edge of the field of view did not exceed 30 m. The weights for including the acceptances from nuclei of different types into the acceptance for the mixed composition were chosen so that the experimental  $\eta$  distribution is described well by the model one. The next approximation to the spectrum of all nuclei, which takes into account the deviation of the spectrum from a power law with the exponent of  $-3.0$ , was obtained after integrating the latter model distribution over bins of the experimental histogram and dividing the experimental histogram by the model one. The result of reconstructing the spectrum of all PCR nuclei is given in Section 6.1.

### 5.7. Separation of PCR Nuclear Groups

In this study, the technique for studying the PCR nuclear composition is based on the use of the SDF slope index  $\eta$  of EAS CL, which makes it possible to single out some relatively light nuclei against the background of the PCR heavy component [52]. Indeed, the total cross section of interaction between light nuclei and nitrogen or oxygen in air is smaller than that for the case of heavier nuclei; therefore, some showers initiated by light nuclei develop deeper and have larger  $\eta$  values. The slope index allows one to develop criteria of individual separation of the PCR nuclear groups. In addition, in contrast to the parameter  $X_{\max}$ , the  $\eta$  value can be directly measured. In this study, model protons were the “light” component, whereas iron nuclei were the “heavy” component. The classification  $p/Fe$  was performed for events of

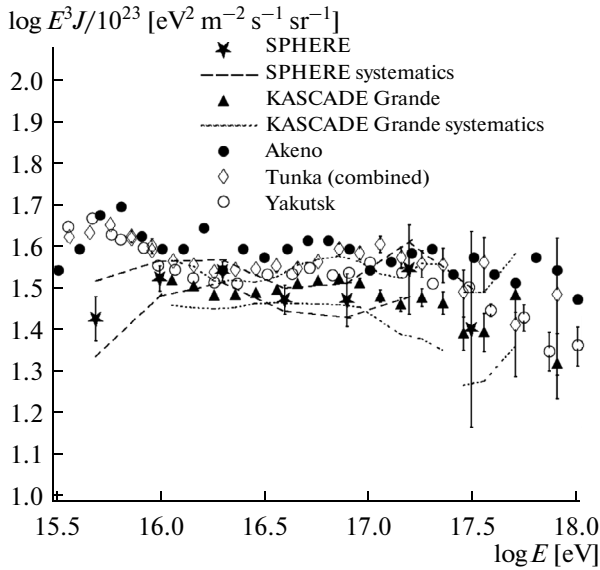


**Fig. 30.** Differential energy spectrum based on data obtained in 2011–2013: (asterisks) SPHERE-2, (triangles) KASCADE-Grande, (dots) Akeno, (diamonds) Tunka-133, and (circles) Yakutsk. Dashed lines indicate systematic errors.

exposure 2012 with reconstructed zenith angles in the range from  $0^\circ$  to  $40^\circ$ .

## 6. RESULTS OF THE SPHERE-2 EXPERIMENT

The main results of measuring the energy spectrum and estimating the PCR composition are based on the data obtained in the expeditions of 2011–2013. The laboratory investigations of the characteristics of sensitivity of the SPHERE-2 setup detector and the electronic measuring system were also carried out during this time interval. Based on the data of laboratory investigations, the refinement and improvement of the procedure of reconstructing the PCR characteristics are under way. The results reported below are not final.

### 6.1. Energy Spectrum

The spectrum of all PCR nuclei reconstructed based on the data obtained during exposure 2011–2013 of the SPHERE-2 experiment is indicated by asterisks in Fig. 30. The statistical and systematic errors of the measurements of the spectrum are shown in the figure. Several main sources of the systematic errors in determining the spectrum were taken into account:

- (i) Migration of events between energy bins (dominates at energies above 20 PeV).
- (ii) Statistical and systematic errors in calculating the acceptance.

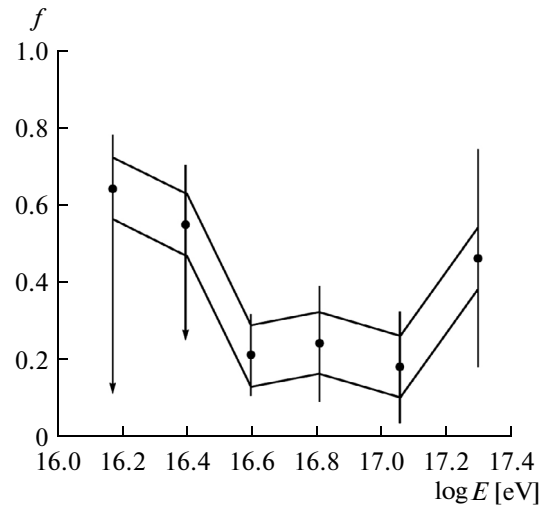


**Fig. 31.** (circles) Dependence of the fraction  $f$  of light nuclei on  $\log(E_0)$  based on data obtained during exposure 2012 of the SPHERE-2 experiment and statistical errors of this parameter. Broken lines show a typical size of the systematic error in estimating  $f$ . Arrows indicate additional uncertainties due to the threshold effects.

(iii) Dependence of the shape of the spectrum on the PCR composition (dominates at energies below 20 PeV).

(iv) Discreteness of the energy of model events.

(v) Uncertainty in estimating the shower zenith angle.

The two latter error sources can be neglected.

The results of the Akeno, KASCADE-Grande, Tunka-133, and Yakutsk experiments are also shown in Fig. 30 for comparison. The statistical errors of the Akeno spectrum are comparable with the marker diameter; dotted lines indicate the systematic errors of the KASCADE-Grande spectrum.

### 6.2. Estimation of the PCR Composition

The dependence of the fraction  $f$  of light nuclei in the total PCR composition on the decimal logarithm of energy according to the data of the SPHERE-2 experiment is shown by circles with statistical errors in Fig. 31. The estimated systematic uncertainties are indicated by solid lines. The  $f$  value in the first two energy bins is distorted by threshold effects. A typical value of the additional uncertainty arising in this case is indicated by arrows. Based on the data shown in Fig. 31, the energy-averaged fraction of light nuclei in the PCR composition with the energy of 30–150 PeV was estimated to be  $(21 \pm 11)\%$ . On the assumption that the heavy component contains only iron nuclei, the mean logarithm of the PCR atomic weight is  $\langle \ln A \rangle = 3.20 \pm 0.45$ ; in the case of silicon nuclei,  $\langle \ln A \rangle = 2.65 \pm 0.37$ ; and in the case of nitrogen nuclei,

$\langle \ln A \rangle = 2.10 \pm 0.30$ . The  $\ln A$  values from 2 to 3 in the energy range under study do not contradict the conclusions of [25] (Fig. 17).

The systematic errors, which can affect the results shown in Figs. 30 and 31, are currently analyzed in more details.

## 7. PROSPECTS OF DEVELOPING THE SPHERE EXPERIMENT

The experimental results obtained are an important stage in development of the technique of detecting reflected EAS CL. Despite low statistical accuracy, the result is in good agreement with the data of other systems. A high methodical accuracy of the performed measurements provides good prospects of developing new experimental projects. Proceeding from the experience of using the SPHERE-1 and SPHERE-2 setups, the systems with better possibilities (as compared with not only these balloon detectors but also many ground-based ones) can be developed. Advantages of the used technique and progress in microelectronics already provide possibilities for designing a compact detector of reflected EAS CL with a large fiducial detection area, wide solid angle of view, and high spatial resolution. Indeed, having compared a ground-based system with the fiducial area of about 10 km<sup>2</sup> including 2500 detectors, service infrastructure, etc., and a compact balloon detector with a mass below 150 kg having similar characteristics, one can clearly see the differences in material and labor expenditures to obtain comparable scientific results. Expenses for systems with a large detection area are several tens (or even hundreds) of times higher.

### 7.1. Problems for New Experiments

What possible applications of this technique appear to be most promising to date? Three regions can arbitrarily be selected in the spectrum of PCRs with ultrahigh energies:

- (i) Region of relatively low ( $10^{15}$ – $10^{17}$  eV) energies.
- (ii) Region of “intermediate” ( $10^{17}$ – $10^{19}$  eV) energies.
- (iii) Region of extremely high energies (above  $10^{19}$  eV).

Sources of superhigh energy cosmic rays are still unknown; however, most researchers suggest that the overwhelming majority of observed nuclei with the energy below  $10^{17}$  eV have a galactic nature, nuclei with the energy above  $10^{19}$  eV are almost entirely generated by extragalactic sources, and the energy range of  $10^{17}$ – $10^{19}$  eV is a transition region from galactic to extragalactic sources. The experimental studies of 2005–2013 on the composition of superhigh energy PCRs can be arbitrarily divided into three periods:

**2005–2007.** The results of the KASCADE experimental on the PCR composition in the energy range of  $10^{15}$ – $10^{17}$  eV are most interesting.

**2008–2010.** Researchers are focused on the range of extremely high energies (HiRes and Auger experiments).

**2011–2013.** Many studies are devoted to intermediate energies and their results are most widely discussed (in particular, KASCADE-Grande results and some results of the HiRes, Auger, and Telescope Array experiments).

Note that there is no detailed information on the PCR nuclear composition in all above-mentioned energy ranges. The International Cosmic Ray Conference ICRC2013 in Rio de Janeiro gave rise to a new tendency: again there are studies performed at relatively low ( $10^{15}$ – $10^{17}$  eV) and ultrahigh (above  $10^{19}$  eV) energies. Among all presentations for ICRC2013, a great attention was paid to the report of the KASCADE-Grande collaboration devoted to separation of nuclear groups in the energy range of  $3 \times 10^{16}$ – $10^{18}$  eV [95].

According to the KASCADE-Grande results, the spectrum of the “heavy” component has a “knee” kink at the energy of  $8 \times 10^{16}$  eV, whereas the spectrum of the “light” component has an “ankle” kink at the energy of  $1.2 \times 10^{17}$  eV. A feature in the “heavy” component spectrum was expected in many popular versions of the galactic cosmic ray model. At the same time, the result of measuring the shape of the “light” component spectrum was rather unexpected. All above results should be verified by independent methods.

The method described in this review can be effectively applied in the aforementioned energy ranges. To use all advantages of the technique, it is proposed to design two independent systems for studying cosmic rays in different energy ranges:  $10^{15}$ – $10^{18}$  eV and  $10^{17}$ – $10^{20}$  eV. To investigate the range of  $10^{15}$ – $10^{18}$  eV, a system (similar to the SPHERE-2 setup) with a higher sensitivity and a higher spatial resolution is currently being developed. The working title of the promising system is SPHERE-HD (abbreviated high definition). To analyze the range of  $10^{17}$ – $10^{20}$  eV, a very light (less than 50 kg) and compact ( $\sim 50 \times 50 \times 80$  cm) detector is designed to be lifted to an altitude of 25–40 km by a free balloon in Antarctica.

### 7.2. Design of the High-Definition SPHERE-HD Setup

The energy range of  $10^{15}$ – $10^{18}$  eV is a transition from galactic cosmic rays to extragalactic. A change in the PCR spectrum slope at about  $3 \times 10^{15}$  eV was found in this range more than 50 years ago. However, new peculiarities in the spectrum continue to be revealed (see Section 7.1). In this context, it is interesting to find the origin of these nonuniformities. The main reason is very likely to be a change in the PCR composition. The modern methods make it possible to either estimate

the average PCR composition (see Section 6.2) or select “light” and “heavy” groups. The estimations are mainly performed on the basis of the data of reconstructing the depth of the EAS development maximum using the methods of simulating the processes of cascade occurrence and development. The groups can be selected only after processing a large amount of experimental data because of large methodical errors of ground-based systems. The technique considered in this review makes it possible to achieve higher measurement accuracy in comparison with techniques of ground-based systems. The new high-definition SPHERE-HD setup is designed to fully implement all possibilities of the method. It is believed that the SPHERE-HD setup will have the following parameters:

- (i) Sensitive area of the diaphragm input window of the optical system is  $1\text{--}1.5\text{ m}^2$ .
- (ii) Number of photodetectors in the array is 2–2.5 thousands.
- (iii) Altitude is up to 4 km.
- (iv) Monitoring of the atmosphere density and transparency.
- (v) Laser monitoring of the snow reflectance.

These characteristics of the SPHERE-HD setup will make it possible to reduce the detection energy threshold to 3–5 PeV. As a result, the amount of experimental data will increase several tens of times. The spatial resolution of recording SDF of EAS CL will vary from 15 to 60 m depending on the setup altitude above the snow surface.

At energies of  $10^{17}\text{--}10^{18}$  eV, the maximum of EAS cascade development is at an altitude of several kilometers above the Earth surface. A unique position of the system will allow one to directly monitor parameters (density and transparency) of atmosphere where EAS develops. The laser monitoring of the snow reflectance will increase the accuracy of measuring the EAS CL density.

### 7.3. Project of Technique Application in Antarctica

Investigation of cosmic rays with extremely high energies ( $E_0 > 10^{19}$  eV) is one of the most interesting problems in modern astrophysics. Currently, several large ground-based experimental setups operate in the range of  $10^{18}\text{--}10^{20}$  eV [13–15, 20, 21]; however, their measurement results are in poor agreement because of the inherent systematic errors in the experiments. In this energy range, the EAS development maximum is near the sea level, and its depth is difficult to study using ground-based systems. A geometric assessment of the balloon experiment will allow one to determine its position with a higher accuracy.

It is suggested that the SPHERE-Antarctica setup will consist of a system of flat lenses about 0.5 m in diameter with a correction of spherical aberration focusing EAS light on a spherical photodetector 30–

50 cm in diameter. The detector is proposed to consist of 1000 semiconductor detectors with the quantum yield at the maximum  $\eta_{\text{max}} = 0.4$ . The average effective quantum yield for the wavelength range of 300–600 nm is  $\eta = 0.27$ . The total opening angle of the entire system is  $\sim 1$  sr. From an altitude of 25–30 km each detector cell will observe a surface area of  $1 \times 1$  km. The threshold energies of detecting EAS fluorescent light and EAS CL will be  $2 \times 10^{18}$  eV and  $2 \times 10^{17}$  eV, respectively. The system weight is estimated to be 50 kg.

During a 90-day flight during the polar night at an altitude of 25 km above Antarctica, one setup can detect  $\sim 1.2 \times 10^5$  EASs with the energy above  $10^{18}$  eV and about thousand events with the energy  $\geq 10^{19}$  eV. Such a long-term flight is due to unique wind conditions in Antarctica in winter: circumpolar air circulation in the middle of Antarctica and only slight presence of wind in the polar region. If a group of several tens or hundreds of these devices is launched, the accumulated statistics may increase by a factor of 10–100.

The technique of measuring the PCR energy spectrum and mass composition in the energy range of  $10^{18}\text{--}10^{20}$  eV, which is planned to implement in the SPHERE-Antarctica experiment, appears to be most adequate for the stated problem because the total CL flux reflected from the snow surface depends weakly on the primary-nucleus type, and the fraction of EAS CL is extremely small when recording the EAS cascade curve shape based on fluorescent light. Thus, the problem of separating Cherenkov and fluorescent lights, typical of ground-based systems, is solved due to the difference in arrival times of these components of the EAS at the detector.

A high accuracy of determining the zenith angle of EAS arrival in the SPHERE-Antarctica experiment will be provided by measuring not only amplitude but also time structure of pulses, as well as time intervals between pulses of EAS CL and FL. Recording of several points in the cascade curve makes it possible to determine the depth of EAS development maximum and the zenith angle of inclination of the EAS axis. Using these data, one can analyze the PCR mass composition and increase the accuracy of reconstructing the PCR energy spectrum.

## CONCLUSIONS

In this paper, we presented the most complete review of experimental and calculation studies on development of the technique of observing reflected EAS CL. The methods of reconstructing the PCR spectrum and nuclear composition using different EAS components were considered. Although many studies were devoted to superhigh energy PCRs during the last few decades, the results of measuring the spectrum and, especially, mass composition are contradictory. This leads to the need for developing new methods of detection and analysis.

The technique under consideration has a number of important advantages. In particular, it allows one to detect EAS CL directly from the paraxial shower region, which is especially sensitive to the PCR nuclear composition. In addition, investigations of the same spectral regions from different altitudes make it possible to estimate the systematic errors in a more correct way. The optical properties of the snow surface served as a screen are rather stable and have been studied fairly well.

The first observations of reflected EAS CL carried out in the 1980s–early 1990s did not make it possible to reconstruct the energy spectrum in detail and, all the more, study the PCR mass composition. Currently, the most advanced detector employing this method is the SPHERE-2 telescope. In this paper, the experimental equipment was described in detail for the first time and the technique of its relative and absolute calibration was considered. Since the detector of the SPHERE experiment is a compact device, the direct calibration of the measuring channel sensitivity is performed on-line, which is very important for the problem of studying the PCR mass composition (however, it has been implemented in none ground-based experiment on EAS CL).

In this study, a particular attention was paid to the modern technique of simulating the detector response and analyzing data in the SPHERE experiment. The use of a sample of model showers calculated by the complete direct statistical simulation made it possible to correctly describe fluctuations in EAS development. Specific features of model responses of the SPHERE-2 detector were described. The technique of calculating the fiducial acceptance of detecting showers was considered. It was shown that the main difficulty in reconstructing the spectrum of all nuclei (the dependence of the fiducial acceptance on the nuclear composition) can successfully be overcome using information about the shape of the SDF of showers detected in the experiment.

The results of analyzing the experimental data were obtained during the observations of 2008–2013 at Lake Baikal (the spectrum of all nuclei and estimated fraction of light nuclei as a function of energy). Currently, systematic errors of these results are analyzed in more detail.

Lines of development of the technique of detecting reflected EAS CL were proposed. A large contribution to investigation of the PCR composition in the energy range of  $10^{15}$ – $10^{18}$  eV will be made by the high-definition SPHERE-HD setup. For studies in the range of  $10^{18}$ – $10^{20}$  eV, it is proposed to construct (using up-to-date equipment) a new balloon system with a small size and weight, which can stay at an altitude of 25–30 km above the Antarctica surface covered with ice and snow for 1–3 months during the polar night and detect both EAS FL in atmosphere and the total EAS CL flux reflected from the snow surface. This system would be

a unique instrument for studying a celestial sphere of the southern hemisphere, which cannot be observed from the territory of the Russian Federation.

## ACKNOWLEDGMENTS

This study was supported by the Russian Foundation for Basic Research, project nos. 11-02-01475-a, 12-02-10007-k, and 13-02-00470-a) and the basic research program “Fundamental Properties of Matter and Astrophysics” of the Presidium of the Russian Academy of Sciences. The fiducial acceptance of detecting showers was calculated using the computing cluster at the Skobeltsyn Institute of Nuclear Physics, Moscow State University (SINP MSU).

## REFERENCES

1. V. L. Ginzburg, “Astrophysics of cosmic rays (history and overview),” *Usp. Fiz. Nauk* **166** (2), 169–183 (1996).
2. A. A. Moiseev, “Gamma-ray large area space telescope: mission overview,” *Nucl. Instrum. Methods Phys. Res., A* **588** (1–2), 41–47 (2008).
3. A. Neronov, D. V. Semikoz, and A. M. Taylor, “Low-energy break in the spectrum of galactic cosmic rays,” *Phys. Rev. Lett.* **108**, 051105 (2012).
4. M. Kachelrieß and S. Ostapchenko, “Deriving the cosmic ray spectrum from gamma-ray observations,” *Phys. Rev. D* **86**, 043004 (2012).
5. (The RUNJOB Collab.) V. A. Derbina, V. I. Galkin, M. Hareyama, Y. Hirakawa, Y. Horiuchi, M. Ichimura, N. Inoue, E. Kamioka, T. Kobayashi, V. V. Kopenkin, S. Kuramata, A. K. Managadze, H. Matsutani, N. P. Misnikova, R. A. Mukhamedshin, S. Nagasawa, R. Nakano, M. Namiki, M. Nakazawa, H. Nanjo, S. N. Nazarov, S. Ohata, H. Ohtomo, V. I. Osedlo, D. S. Oshuev, P. A. Publichenko, I. V. Rakobolskaya, T. M. Roganova, C. Saito, G. P. Sazhina, H. Semba, T. Shibata, D. Shuto, H. Sugimoto, R. Suzuki, L. G. Sveshnikova, V. M. Taran, N. Yajima, T. Yamagami, I. V. Yashin, E. A. Zamchalova, G. T. Zatsepin, and I. S. Zayarnaya, “Cosmic-ray spectra and composition in the energy range of 10–1000 TeV per particle obtained by the RUNJOB experiment,” *Astrophys. J., Lett.* **628** (1), L41 (2005).
6. K. Asakimori, T. H. Burnett, M. L. Cherry, K. Chevli, M. J. Christ, S. Dake, J. H. Derrickson, W. F. Fountain, M. Fuki, J. C. Gregory, T. Hayashi, R. Holynski, J. Iwai, A. Iyono, J. Johnson, M. Kobayashi, J. Lord, O. Miyamura, K. H. Moon, B. S. Nilsen, H. Oda, T. Ogata, E. D. Olson, T. A. Parnell, F. E. Roberts, K. Sengupta, T. Shiina, S. C. Strausz, T. Sugitate, Y. Takahashi, T. Tominaga, J. W. Watts, J. P. Wefel, B. Wilczynska, H. Wilczynski, R. J. Wilkes, W. Wolter, H. Yokomi, and E. Zager, “Cosmic-ray proton and helium spectra: results from the JACEE experiment,” *Astrophys. J.* **502** (1), 278 (1998).
7. K. Ya. Kondrat’ev, *Albedo and Angular Characteristics of Reflection of the Underlying Surface and Clouds* (Gidrometeoizdat, Leningrad, 1981) [in Russian].

8. S. G. Warren, "Optical properties of snow," *Rev. Geophys. Space Phys.* **20**, 67–89 (1980).
9. A. A. Kokhanovsky, *Light Scattering Reviews 7: Radiative Transfer and Optical Properties of Atmosphere and Underlying Surface* (Springer, 2012), pp. 151–187.
10. J. V. Jelley, *Čerenkov Radiation and Its Applications* (Pergamon Press, 1958).
11. V. Antonov, O. Kruglov, and V. Kuz'min, "Instruments for measuring optical parameters and characteristics of light-emitting diodes," *Poluprovodn. Svetotekhnika* **3**, 26–31 (2010).
12. M. M. Gurevich, *Photometry: Theory, Methods, and Instruments* (Energoatomizdat, Leningrad, 1983) [in Russian].
13. M. Unger and E. J. Ahn, "Inferences about the mass composition of cosmic rays from data on the depth of maximum at the Auger Observatory," in *Proceedings of 33rd ICRC, Rio de Janeiro, 2013*.
14. Yoshiki Tsunesada, "Telescope array composition measurements," in *Proceedings of 33rd ICRC, Rio de Janeiro, 2013*.
15. Anatoly Ivanov, "The Yakutsk array experiment: main results and future directions," *EPJ Web Conf.* **53**, 04003–04013 (2013).
16. S. P. Knurenko, "Cosmic ray spectrum in the energy range  $1.0E15$ – $1.0E18$  eV and the second knee according to the small Cherenkov setup at the Yakutsk EAS array," in *Proceedings of 33rd International Cosmic Ray Conference, Rio de Janeiro, Brazil, 2013*.
17. G. V. Kulikov and G. B. Christiansen, "On spectrum of extensive air showers based on number of particles," *Zh. Eksp. Teor. Fiz.* **35** (3(9)), 635–640 (1958).
18. W. D. Apel, J. C. Arteaga-Velázquez, K. Bekk, M. Bertina, J. Blümer, H. Bozdog, I. M. Brancus, P. Buchholz, E. Cantoni, A. Chiavassa, F. Cossavella, K. Daumiller, V. de Souza, F. Di Pierro, P. Doll, R. Engel, J. Engler, M. Finger, D. Fuhrmann, P. L. Ghia, H. J. Gils, R. Glasstetter, C. Grupen, A. Haungs, D. Heck, J. R. Hörandel, D. Huber, T. Huege, K.-H. Kampert, D. Kang, D. Kickelbick, H. O. Klages, K. Link, P. Łuczak, M. Ludwig, H. J. Mathes, H. J. Mayer, M. Melissas, J. Milke, B. Mitrica, C. Morello, G. Navarra, J. Oehlschläger, S. Ostapchenko, S. Over, N. Palmieri, M. Petcu, T. Pierog, H. Rebel, M. Roth, H. Schieler, F. G. Schröder, O. Sima, G. Toma, G. C. Trincherro, H. Ulrich, A. Weindl, J. Wochele, M. Wommer, and J. Zabierowski, "The spectrum of high-energy cosmic rays measured with KASCADE-Grande," *Astropart. Phys.* **36** (1), 183–194 (2012).
19. M. Takeda, N. Sakaki, K. Honda, M. Chikawa, M. Fukushima, N. Hayashida, N. Inoue, K. Kadota, F. Kakimoto, K. Kamata, S. Kawaguchi, S. Kawakami, Y. Kawasaki, N. Kawasumi, A. M. Mahrous, K. Mase, S. Mizobuchi, Y. Morizane, M. Nagano, H. Ohoka, S. Osone, M. Sasaki, M. Sasano, H. M. Shimizu, K. Shinozaki, M. Teshima, R. Torii, I. Tsushima, Y. Uchihori, T. Yamamoto, S. Yoshida, and H. Yoshii, "Energy determination in the Akeno Giant Air Shower Array experiment," *Astropart. Phys.* **19** (4), 447–462 (2003).
20. Douglas Bergman, "Telescope array measurements of the UHECR energy spectrum," in *Proceedings of 33rd ICRC, Rio de Janeiro, 2013*.
21. Alexander Schulz, "The measurement of the energy spectrum of cosmic rays above  $3 \times 10^{17}$  eV with the Pierre Auger Observatory," in *Proceedings of 33rd ICRC, Rio de Janeiro, 2013*.
22. (The Pierre Auger Collab.) P. Abreu, M. Aglietta, M. Ahlers, E. J. Ahn, I. F. M. Albuquerque, D. Allard, I. Allekotte, J. Allen, P. Allison, A. Almela, J. Alvarez Castillo, J. Alvarez-Muñiz, R. Alves Batista, M. Ambrosio, A. Aminaei, L. Anchordoqui, S. Andringa, T. Antičić, C. Aramo, E. Arganda, F. Arqueros, H. Asorey, P. Assis, J. Aublin, M. Ave, M. Avenier, G. Avila, A. M. Badescu, M. Balzer, K. B. Barber, A. F. Barbosa, R. Bardenet, S. L. C. Barroso, B. Baughman, J. Bäuml, C. Baus, J. J. Beatty, K. H. Becker, A. Bellétoile, J. A. Bellido, S. BenZvi, C. Berat, X. Bertou, P. L. Biermann, P. Billoir, F. Blanco, M. Blanco, C. Bleve, H. Blümer, M. Boháčová, D. Boncioli, C. Bonifazi, R. Bonino, N. Borodai, J. Brack, I. Brancus, P. Brogueira, W. C. Brown, R. Bruijn, P. Buchholz, A. Bueno, L. Buroker, R. E. Burton, K. S. Caballero-Mora, B. Caccianiga, L. Caramete, R. Caruso, A. Castellina, O. Catalano, G. Cataldi, L. Cazon, R. Cester, J. Chauvin, S. H. Cheng, A. Chiavassa, J. A. Chinellato, J. Chirinos Diaz, J. Chudoba, M. Cilmo, R. W. Clay, G. Cocciolo, L. Collica, M. R. Coluccia, R. Conceicao, F. Contreras, H. Cook, M. J. Cooper, J. Coppers, A. Cordier, S. Couto, C. E. Covault, A. Creusot, A. Criss, J. Cronin, A. Curutiu, S. Dagoret-Campagne, R. Dallier, B. Daniel, S. Dasso, K. Daumiller, B. R. Dawson, R. M. de Almeida, M. De Domenico, C. De Donato, S. J. de Jong, G. De La Vega, W. J. M. de Mello, Jr., J. R. T. de Mello Neto, I. De Mitri, V. de Souza, K. D. de Vries, L. del Peral, M. del Rio, O. Deligny, H. Dembinski, N. Dhital, Giulio. C. Di, M. L. Diaz Castro, P. N. Diep, F. Diogo, C. Dobrigkeit, W. Docters, J. C. D'Olivo, P. N. Dong, A. Dorofeev, J. C. dos Anjos, M. T. Dova, D. D'Urso, I. Dutan, J. Ebr, R. Engel, M. Erdmann, C. O. Escobar, J. Espadana, A. Etchegoyen, P. Facal San Luis, H. Falcke, K. Fang, G. Farrar, A. C. Fauth, N. Fazzini, A. P. Ferguson, B. Fick, J. M. Figueira, A. Filevich, A. Filipčić, S. Fliescher, C. E. Fracchiolla, E. D. Fraenkel, O. Fratu, U. Fröhlich, B. Fuchs, R. Gaior, R. F. Gamarra, S. Gambera, B. García, S. T. Garcia Roca, D. Garcia-Gamez, D. Garcia-Pinto, G. Garilli, A. Gascon Bravo, H. Gemmeke, P. L. Ghia, M. Giller, J. Gitto, H. Glass, M. S. Gold, G. Golup, F. Gomez Albarracin, M. Gómez Berisso, P. F. Gómez Vitale, P. Gonçalves, J. G. Gonzalez, B. Gookin, A. Gorgi, P. Gouffon, E. Grashorn, S. Grebe, N. Griffith, A. F. Grillo, Y. Guardincerri, F. Guarino, G. P. Guedes, P. Hansen, D. Harari, T. A. Harrison, J. L. Harton, A. Haungs, T. Hebbeker, D. Heck, A. E. Herve, G. C. Hill, C. Hojvat, N. HOLLON, V. C. Holmes, P. Homola, J. R. Hörandel, P. Horvath, M. Hrabovský, D. Huber, T. Huege, A. Insolia, F. Ionita, A. Italiano, S. Jansen, C. Jarne, S. Jiraskova, M. Josebachuili, K. Kadija, K. H. Kampert, P. Karhan, P. Kasper, I. Katkov, B. Kégl, B. Keilhauer, A. Keivani, J. L. Kelley, E. Kemp, R. M. Kieckhafer, H. O. Klages,

- M. Kleifges, J. Kleinfeller, J. Knapp, D.-H. Koang, K. Kotera, N. Krohm, O. Krömer, D. Kruppke-Hansen, D. Kuempel, J. K. Kulbartz, N. Kunka, G. La Rosa, C. Lachaud, D. LaHurd, L. Latronico, R. Lauer, P. Lautridou, S. Le Coz, M. S. A. B. Leão, D. Lebrun, P. Lebrun, M. A. Leigui de Oliveira, A. Letessier-Selvon, I. Lhenry-Yvon, K. Link, R. López, A. Lopez Agüera, K. Louedec, J. Lozano Bahilo, L. Lu, A. Lucero, M. Ludwig, H. Lyberis, M. C. Maccarone, C. Macolino, S. Maldera, J. Maller, D. Mandat, P. Mantsch, A. G. Mariazzi, J. Marin, V. Marin, I. C. Maris, H. R. Marquez Falcon, G. Marsella, D. Martello, L. Martin, H. Martinez, O. Martínez Bravo, D. Martraire, J. J. Masías Meza, H. J. Mathes, J. Matthews, J. A. J. Matthews, G. Matthiae, D. Maurel, D. Maurizio, P. O. Mazur, G. Medina-Tanco, M. Melissas, D. Melo, E. Menichetti, A. Menshikov, P. Mertsch, S. Messina, C. Meurer, R. Meyhandan, S. Mićanović, M. I. Micheletti, I. A. Minaya, L. Miramonti, L. Molina-Bueno, S. Mollerach, M. Monasor, D. Monnier Ragainne, F. Montanet, B. Morales, C. Morello, E. Moreno, J. C. Moreno, M. Mostafá, C. A. Moura, M. A. Muller, J. G. Müller, M. Münchmeyer, R. Mussa, G. Navarra, J. L. Navarro, S. Navas, P. Necesal, L. Nellen, A. Nelles, J. Neuser, P. T. Nhung, M. Niechciol, L. Niemietz, N. Nierstenhoefer, D. Nitz, D. Nosek, L. Nožka, J. Oehlschläger, A. Olinto, M. Ortiz, N. Pacheco, Selmi-Dei. D. Pakk, M. Palatka, J. Pallotta, N. Palmieri, G. Parente, E. Parizot, A. Parra, S. Pastor, T. Paul, M. Pech, J. Pečala, R. Pelayo, I. M. Pepe, L. Perrone, R. Pesce, E. Petermann, S. Petrerá, A. Petrolini, Y. Petrov, C. Pfendner, R. Piegáia, T. Pierog, P. Pieroni, M. Pimenta, V. Pirronello, M. Platino, M. Plum, V. H. Ponce, M. Pontz, A. Porcelli, P. Privitera, M. Prouza, E. J. Quel, S. Querschfeld, J. Rautenberg, O. Ravel, D. Ravignani, B. Revenu, J. Ridky, S. Riggi, M. Risse, P. Ristori, H. Rivera, V. Rizi, J. Roberts, W. Rodrigues de Carvalho, G. Rodriguez, I. Rodriguez Cabo, J. Rodriguez Martino, J. Rodriguez Rojo, M. D. Rodríguez-Frías, G. Ros, J. Rosado, T. Rossler, M. Roth, B. Rouillé-d'Orfeuill, E. Roulet, A. C. Rovero, C. Rühle, A. Saftoiu, F. Salamida, H. Salazar, F. Salesa Greus, G. Salina, F. Sánchez, C. E. Santo, E. Santos, E. M. Santos, F. Sarazin, B. Sarkar, S. Sarkar, R. Sato, N. Scharf, V. Scherini, H. Schieler, P. Schiffer, A. Schmidt, O. Scholten, H. Schoorlemmer, J. Schovancova, P. Schovánek, F. Schröder, D. Schuster, S. J. Sciutto, M. Scuderi, A. Segreto, M. Settimo, A. Shadkam, R. C. Shellard, I. Sidelnik, G. Sigl, H. H. Silva Lopez, O. Sima, A. Śmiałkowski, R. Šmída, G. R. Snow, P. Sommers, J. Sorokin, H. Spinka, R. Squartini, Y. N. Srivastava, S. Stanic, J. Stapleton, J. Stasielak, M. Stephan, A. Stutz, F. Suarez, T. Suomijärvi, A. D. Supanitsky, T. Šušá, M. S. Sutherland, J. Swain, Z. Szadkowski, M. Szuba, A. Tapia, M. Tartare, O. Taşcau, R. Tcaciuc, N. T. Thao, D. Thomas, J. Tiffenberg, C. Timmermans, W. Tkaczyk, C. J. Todero Peixoto, G. Toma, L. Tomankova, B. Tomé, A. Tonachini, G. Torralba Elipe, P. Travnicek, D. B. Tridapalli, G. Tristram, E. Trovato, M. Tüeros, R. Ulrich, M. Unger, M. Urban, J. F. Valdés Galicia, I. Valiño, L. Valore, G. van Aar, A. M. van den Berg, S. van Vélzen, A. van Vliet, E. Várela, B. Vargas Cárdenas, J. R. Vázquez, R. A. Vázquez, D. Veberič, V. Verzi, J. Vicha, M. Videla, L. Villasenor, H. Wahlberg, P. Wahrlich, O. Wainberg, D. Walz, A. A. Watson, M. Weber, K. Weidenhaupt, A. Weindl, F. Werner, S. Westerhoff, B. J. Whelan, A. Widom, G. Wieczorek, L. Wiencke, B. Wilczyn'ska, H. Wilczyn'ski, M. Will, C. Williams, T. Winchen, M. Wommer, B. Wundheiler, T. Yamamoto, T. Yapici, P. Younk, G. Yuan, A. Yushkov, B. Zamorano Garcia, E. Zas, D. Zavrtnik, M. Zavrtnik, I. Zaw, A. Zepeda, J. Zhou, Y. Zhu, M. Zimbres Silva, and M. Ziolkowski, "Large-scale distribution of arrival directions of cosmic rays detected above  $10^{18}$  eV at the Pierre Auger Observatory," *Astrophys. J., Suppl. Ser. @203@* (2), 34 (2012).
23. M. T. Dova, M. E. Manceñido, A. G. Mariazzi, T. P. McCauley, and A. A. Watson, "The mass composition of cosmic rays near  $10^{18}$  eV as deduced from measurements made at Volcano Ranch," *Astropart. Phys.* **21** (6), 597–607 (2004).
  24. T. Antoni, W. D. Apel, A. F. Badea, K. Bekk, A. Bercuci, J. Blümer, H. Bozdog, I. M. Brancus, A. Chilingarian, K. Daumiller, P. Doll, R. Engel, J. Engler, F. Febler, H. J. Gils, R. Glasstetter, A. Haungs, D. Heck, J. R. Hörandel, K.-H. Kampert, H. O. Klages, G. Maier, H. J. Mathes, H. J. Mayer, J. Milke, M. Müller, R. Obenland, J. Oehlschläger, S. Ostapchenko, M. Petcu, H. Rebel, A. Risse, M. Risse, M. Roth, G. Schatz, H. Schieler, J. Scholz, T. Thouw, H. Ulrich, J. van Buren, A. Vardanyan, A. Weindl, J. Wochele, and J. Zabierowski, "KASCADE measurements of energy spectra for elemental groups of cosmic rays: results and open problems," *Astropart. Phys.* **24** (1-2), 1–25 (2005).
  25. Karl-Heinz Kampert and Michael Unger, "Measurements of the cosmic ray composition with air shower experiments," *Astropart. Phys.* **35** (10), 660–678 (2012).
  26. R. U. Abbasi, T. Abu-Zayyad, G. Archbold, R. Atkins, J. Bellido, K. Belov, J. W. Belz, S. BenZvi, D. R. Bergman, J. Boyer, G. W. Burt, Z. Cao, R. Clay, B. M. Connolly, B. Dawson, W. Deng, Y. Fedorova, J. Findlay, C. B. Finley, W. F. Hanlon, G. A. Hughes, P. Huntmeyer, C. C. H. Jui, K. Kim, M. A. Kirn, B. Knapp, E. C. Loh, M. M. Maetas, K. Martens, G. Martin, N. Manago, E. J. Mannel, J. A. J. Matthews, J. N. Matthews, A. O'Neill, L. Perera, K. Reil, R. Riehle, M. D. Roberts, M. Sasaki, M. Seman, S. R. Schnetzer, K. Simpson, J. D. Smith, R. Snow, P. Sokolsky, C. Song, R. W. Springer, B. T. Stokes, J. R. Thomas, S. B. Thomas, G. B. Thomson, S. Westerhoff, L. R. Wiencke, and A. Zech, "A study of the composition of ultra-high-energy cosmic rays using the high-resolution Fly's Eye," *Astrophys. J.* **622** (2), 910 (2005).
  27. T. Huege, "The renaissance of radio detection of cosmic rays," in *Proceedings of 33rd ICRC, Rio de Janeiro, 2013*.
  28. W. D. Apel, J. C. Arteaga, L. Bähren, K. Bekk, M. Bertina, P. L. Biermann, J. Blümer, H. Bozdog, I. M. Brancus, P. Buchholz, E. Cantoni, A. Chiavassa, K. Daumiller, V. de Souza, F. Di Pierro, P. Doll, R. Engel, H. Falcke, M. Finger, B. Fuchs, D. Fuhrmann, H. Gemmeke, C. Grupen, A. Haungs, D. Heck, J. R. Hörandel, A. Horneffer, D. Huber, T. Huege, P. G. Isar, K.-H. Kampert, D. Kang, O. Krömer,

- J. Kuijpers, K. Link, P. Łuczak, M. Ludwig, H. J. Mathes, M. Melissas, C. Morello, J. Oehlschläger, N. Palmieri, T. Pierog, J. Rautenberg, H. Rebel, M. Roth, C. Rühle, A. Saftoiu, H. Schieler, A. Schmidt, F. G. Schröder, O. Sima, G. Toma, G. C. Trinchero, A. Weindl, J. Wochele, M. Wommer, J. Zabierowski, and J. A. Zensus, “Experimental evidence for the sensitivity of the air-shower radio signal to the longitudinal shower development,” *Phys. Rev. D* **85**, 071101 (2012).
29. P. W. Gorham, N. G. Lehtinen, G. S. Varner, J. J. Beatty, A. Connolly, P. Chen, M. E. Conde, W. Gai, C. Hast, C. L. Hebert, C. Miki, R. Konecny, J. Kowalski, J. Ng, J. G. Power, K. Reil, L. Ruckman, D. Saltzberg, B. T. Stokes, and D. Walz, “Observations of microwave continuum emission from air shower plasmas,” *Phys. Rev. D* **78**, 032007 (2008).
30. T. Yamamoto, “Development of microwave telescopes for detection of molecular bremsstrahlung radiation from EAS of UHECR,” in *Proceedings of 32th ICRC, V. 3, Beijing, 2011*, p. 227.
31. Dmitry Zaborov, “An analysis approach to acoustic detection of extensive atmospheric showers,” *Int. J. Mod. Phys. A* **21** (supp01), 87–91 (2006).
32. (The IceCube Collab.) R. Abbasi, Y. Abdou, M. Ackermann, J. Adams, J. A. Aguilar, M. Ahlers, D. Altmann, K. Andeen, J. Auffenberg, X. Bai, M. Baker, S. W. Barwick, V. Baum, R. Bay, K. Beattie, J. J. Beatty, S. Bechet, J. Becker Tjus, K.-H. Becker, M. Bell, M. L. Benabderrahmane, S. BenZvi, J. Berdermann, P. Berghaus, D. Berley, E. Bernardini, D. Bertrand, D. Z. Besson, D. Bindig, M. Bissok, E. Blaufuss, J. Blumenthal, D. J. Boersma, C. Böhm, D. Bose, S. Böser, O. Botner, L. Brayeur, A. M. Brown, R. Bruijn, J. Brunner, S. Buitink, K. S. Caballero-Mora, M. Carson, J. Casey, M. Casier, D. Chirkin, B. Christy, F. Clevermann, S. Cohen, D. F. Cowen, A. H. Cruz Silva, M. Danninger, J. Daughhetee, J. C. Davis, C. De Clercq, F. Descamps, P. Desiati, G. de Vries-Uiterweerd, T. DeYoung, J. C. Díaz-Vélez, J. Dreyer, J. P. Dumm, M. Dunkman, R. Eagan, J. Eisch, R. W. Ellsworth, O. Engdegard, S. Euler, P. A. Evenson, O. Fadiran, A. R. Fazely, A. Fedynitch, J. Feintzeig, T. Feusels, K. Filimonov, C. Finley, T. Fischer-Wasels, S. Flis, A. Franckowiak, R. Franke, K. Frantzen, T. Fuchs, T. K. Gaisser, J. Gallagher, L. Gerhardt, L. Gladstone, T. Glüsenkamp, A. Goldschmidt, J. A. Goodman, D. Góra, D. Grant, A. Groß, S. Grullon, M. Gurtner, C. Ha, A. Haj Ismail, A. Hallgren, F. Halzen, K. Hanson, D. Heereman, P. Heimann, D. Heinen, K. Helbing, R. Hellauer, S. Hickford, G. C. Hill, K. D. Hoffman, R. Hoffmann, A. Homeier, K. Hoshina, W. Huelsnitz, P. O. Hulth, K. Hultqvist, S. Hussain, A. Ishihara, E. Jacobi, J. Jacobsen, G. S. Japaridze, O. Jlelati, H. Johansson, A. Kappes, T. Karg, A. Karle, J. Kiryluk, F. Kislak, J. Kläs, S. R. Klein, J.-H. Köhne, G. Kohnen, H. Kolanoski, L. Köpke, C. Kopper, S. Kopper, D. J. Koskinen, M. Kowalski, M. Krasberg, G. Kroll, J. Kunnen, N. Kurahashi, T. Kuwabara, M. Labare, K. Laihem, H. Landsman, M. J. Larson, R. Lauer, M. Lesiak-Bzdak, J. Lünemann, J. Madsen, R. Maruyama, K. Mase, H. S. Matis, F. McNally, K. Meagher, M. Merck, P. Mészáros, T. Meures, S. Miarecki, E. Middell, N. Milke, J. Miller, L. Mohrmann, T. Montaruli, R. Morse, S. M. Movit, R. Nahnauer, U. Naumann, S. C. Nowicki, D. R. Nygren, A. Oberlacke, S. Odrowski, A. Olivas, M. Olivo, A. O’Murchadha, S. Panknin, L. Paul, J. A. Pepper, C. Pérez de los Heros, D. Pieloth, N. Pirk, J. Posselt, P. B. Price, G. T. Przybylski, L. Rädcl, K. Rawlins, P. Redl, E. Resconi, W. Rhode, M. Ribordy, M. Richman, B. Riedel, J. P. Rodrigues, F. Rothmaier, C. Rott, T. Ruhe, D. Rutledge, B. Ruzybayev, D. Ryckbosch, S. M. Saba, T. Salameh, H.-G. Sander, M. Santander, S. Sarkar, K. Schatto, M. Scheel, F. Scheriau, T. Schmidt, M. Schmitz, S. Schoenen, S. Schöneberg, L. Schönherr, A. Schönwald, A. Schukraft, L. Schulte, O. Schulz, D. Seckel, S. H. Seo, Y. Sestayo, S. Seunarine, M. W. E. Smith, M. Soiron, D. Soldin, G. M. Spiczak, C. Spiering, M. Stamatikos, T. Stanev, A. Stasik, T. Stezelberger, R. G. Stokstad, A. Stöbl, E. A. Strahler, R. Ström, G. W. Sullivan, H. Taavola, I. Taboada, A. Tamburro, S. Ter-Antonyan, S. Tilav, P. A. Toale, S. Toscano, M. Usner, N. van Eijndhoven, D. van der Drift, A. Van Overloop, J. van Santen, M. Vehringer, M. Voge, C. Walck, T. Waldenmaier, M. Wallraff, M. Walter, R. Wasserman, Ch. Weaver, C. Wendt, S. Westerhoff, N. Whitehorn, K. Wiebe, C. H. Wiebusch, D. R. Williams, H. Wissing, M. Wolf, T. R. Wood, K. Woschnagg, C. Xu, D. L. Xu, X. W. Xu, J. P. Yanez, G. Yodh, S. Yoshida, P. Zarzhitsky, J. Ziemann, A. Zilles, and M. Zoll, “Cosmic ray composition and energy spectrum from 1–30 PeV using the 40-string configuration of IceTop and IceCube,” *Astropart. Phys.* **42**, 15–32 (2013).
33. (The IceCube Collab.) M. G. Aartsen, R. Abbasi, Y. Abdou, M. Ackermann, J. Adams, J. A. Aguilar, M. Ahlers, D. Altmann, J. Auffenberg, X. Bai, M. Baker, S. W. Barwick, V. Baum, R. Bay, J. J. Beatty, S. Bechet, J. Becker Tjus, K.-H. Becker, M. L. Benabderrahmane, S. BenZvi, P. Berghaus, D. Berley, E. Bernardini, A. Bernhard, D. Bertrand, D. Z. Besson, G. Binder, D. Bindig, M. Bissok, E. Blaufuss, J. Blumenthal, D. J. Boersma, S. Bohachuk, C. Böhm, D. Bose, S. Böser, O. Botner, L. Brayeur, H.-P. Bretz, A. M. Brown, R. Bruijn, J. Brunner, M. Carson, J. Casey, M. Casier, D. Chirkin, A. Christov, B. Christy, K. Clark, F. Clevermann, S. Coenders, S. Cohen, D. F. Cowen, A. H. Cruz Silva, M. Danninger, J. Daughhetee, J. C. Davis, C. De Clercq, S. De Ridder, P. Desiati, K. D. de Vries, M. de With, T. DeYoung, J. C. Díaz-Vélez, M. Dunkman, R. Eagan, B. Eberhardt, J. Eisch, R. W. Ellsworth, S. Euler, P. A. Evenson, O. Fadiran, A. R. Fazely, A. Fedynitch, J. Feintzeig, T. Feusels, K. Filimonov, C. Finley, T. Fischer-Wasels, S. Flis, A. Franckowiak, K. Frantzen, T. Fuchs, T. K. Gaisser, J. Gallagher, L. Gerhardt, L. Gladstone, T. Glüsenkamp, A. Goldschmidt, G. Golup, J. G. Gonzalez, J. A. Goodman, D. Góra, D. T. Grandmont, D. Grant, A. Groß, C. Ha, A. Haj Ismail, P. Hallen, A. Hallgren, F. Halzen, K. Hanson, D. Heereman, D. Heinen, K. Helbing, R. Hellauer, S. Hickford, G. C. Hill, K. D. Hoffman, R. Hoffmann, A. Homeier, K. Hoshina, W. Huelsnitz, P. O. Hulth, K. Hultqvist, S. Hussain, A. Ishihara, E. Jacobi, J. Jacobsen, K. Jagielski, G. S. Japaridze, K. Jero, O. Jlelati, B. Kaminsky, A. Kappes, T. Karg, A. Karle, J. L. Kelley, J. Kiryluk, J. Kläs, S. R. Klein,

- J.-H. Köhne, G. Kohnen, H. Kolanoski, L. Köpke, C. Kopper, S. Kopper, D. J. Koskinen, M. Kowalski, M. Krasberg, K. Krings, G. Kroll, J. Kunnen, N. Kura-hashi, T. Kuwabara, M. Labare, H. Landsman, M. J. Larson, M. Lesiak-Bzdak, M. Leuermann, J. Leute, J. Lünemann, O. Maciias, J. Madsen, G. Maggi, R. Maruyama, K. Mase, H. S. Matis, F. McNally, K. Meagher, M. Merck, T. Meures, S. Miarecki, E. Middell, N. Milke, J. Miller, L. Mohr-mann, T. Montaruli, R. Morse, R. Nahnauer, U. Naumann, H. Niederhausen, S. C. Nowicki, D. R. Nygren, A. Obertacke, S. Odrowski, A. Olivas, A. Omairat, A. O'Murchadha, L. Paul, J. A. Pepper, C. Pérez de los Heros, C. Pfindner, D. Pieloth, E. Pinat, J. Posselt, P. B. Price, G. T. Przybylski, L. Rädcl, M. Rameez, K. Rawlins, P. Redl, R. Reimann, E. Resconi, W. Rhode, M. Ribordy, M. Richman, B. Riedel, J. P. Rodrigues, C. Rott, T. Ruhe, B. Ruzybayev, D. Ryckbosch, S. M. Saba, T. Salameh, H.-G. Sander, M. Santander, S. Sarkar, K. Schatto, F. Scheriau, T. Schmidt, M. Schmitz, S. Schoenen, S. Schöneberg, A. Schönwald, A. Schukraft, L. Schulte, O. Schulz, D. Seckel, Y. Sestayo, S. Seunarine, R. Shanidze, C. Sheremata, M. W. E. Smith, D. Soldin, G. M. Spiczak, C. Spiering, M. Stamatikos, T. Stanev, A. Stasik, T. Stezelberger, R. G. Stokstad, A. Stöbl, E. A. Strahler, R. Ström, G. W. Sullivan, H. Taavola, I. Taboada, A. Tamburro, A. Tepe, S. Ter-Antonyan, G. Tešić, S. Tilav, P. A. Toale, S. Toscano, E. Unger, M. Usner, S. Valle-corsa, N. van Eijndhoven, A. Van Overloop, J. van Santen, M. Véhring, M. Voге, M. Vraeghe, C. Walck, T. Waldenmaier, M. Wallraff, Ch. Weaver, M. Wellons, C. Wendt, S. Westerhoff, N. Whitehorn, K. Wiebe, C. H. Wiebusch, D. R. Williams, H. Wissing, M. Wolf, T. R. Wood, K. Woschnagg, C. Xu, D. L. Xu, X. W. Xu, J. P. Yanez, G. Yodh, S. Yoshida, P. Zarzhitsky, J. Zie-mann, S. Zierke, and M. Zoll, "Measurement of the cosmic ray energy spectrum with IceTop-73," *Phys. Rev. D* **88**, 042004 (2013).
34. Yoshiki Tsunesada, "High energy cosmic rays, rapporteur talk," in *Proceedings of 33rd ICRC, Rio de Janeiro, 2013*.
35. A. P. Garyaka, R. M. Martirosov, S. V. Ter-Antonyan, A. D. Erlykin, N. M. Nikolskaya, Y. A. Gallant, L. W. Jones, and J. Procureur, "An all-particle primary energy spectrum in the 3–200 PeV energy range," *J. Phys. G: Nucl. Part. Phys.* **35** (11), 115201 (2008).
36. M. Nagano, M. Teshima, Y. Matsubara, H. Y. Dai, T. Hara, N. Hayashida, M. Honda, H. Ohoka, and S. Yoshida, "Energy spectrum of primary cosmic rays above  $10^{17.0}$  eV determined from extensive air shower experiments at Akeno," *J. Phys. G: Nucl. Part. Phys.* **18** (2), 423 (1992).
37. M. Amenomori, X. J. Bi, D. Chen, S. W. Cui, L. K. Danzengluobu Ding, X. H. Ding, C. Fan, C. F. Feng, Z. Feng, Z. Y. Feng, X. Y. Gao, Q. X. Geng, H. W. Guo, H. H. He, M. He, K. Hibino, N. Hotta, H. Hu, H. B. Hu, J. Huang, Q. Huang, H. Y. Jia, F. Kajino, K. Kasahara, Y. Katayose, C. Kato, K. Kawata, Labaciren, G. M. Le, A. F. Li, J. Y. Li, Y.-Q. Lou, H. Lu, S. L. Lu, X. R. Meng, K. Mizutani, J. Mu, K. Munakata, A. Nagai, H. Nanjo, M. Nish-izawa, M. Ohnishi, I. Ohta, H. Onuma, T. Ouchi, S. Ozawa, J. R. Ren, T. Saito, T. Y. Saito, M. Sakata, T. K. Sako, M. Shibata, A. Shiomi, T. Shirai, H. Sugim-oto, M. Takita, Y. H. Tan, N. Tateyama, S. Torii, H. Tsuchiya, S. Udo, B. Wang, H. Wang, X. Wang, Y. Wang, Y. G. Wang, H. R. Wu, L. Xue, Y. Yamamoto, C. T. Yan, X. C. Yang, S. Yasue, Z. H. Ye, G. C. Yu, A. F. Yuan, T. Yuda, H. M. Zhang, J. L. Zhang, N. J. Zhang, X. Y. Zhang, Y. Zhang, Y. Zhang, Zhax-isangzhu, and X. X. Zhou, "The all-particle spectrum of primary cosmic rays in the wide energy range from  $10^{14}$  to  $10^{17}$  eV observed with the Tibet-III air-shower array," *Astrophys. J.* **678** (2), 1165–1179 (2008).
38. W. D. Apel, J. C. Arteaga-Velázquez, K. Bekk, M. Ber-taina, J. Blümer, H. Bozdog, I. M. Brancus, P. Buch-holz, E. Cantoni, A. Chiavassa, F. Cossavella, K. Daumiller, V. de Souza, F. Di Piero, P. Doll, R. Engel, J. Engler, M. Finger, D. Fuhrmann, P. L. Ghia, H. J. Gils, R. Glasstetter, C. Grupen, A. Haungs, D. Heck, J. R. Hörandel, D. Huber, T. Huege, P. G. Isar, K.-H. Kampert, D. Kang, H. O. Klages, K. Link, P. Luczak, M. Ludwig, H. J. Mathes, H. J. Mayer, M. Melissas, J. Milke, B. Mitrica, C. Morello, G. Navarra, J. Oehlschlager, S. Ostapchenko, S. Over, N. Palmieri, M. Petcu, T. Pierog, H. Rebel, M. Roth, H. Schieler, F. G. Schröder, O. Sima, G. Toma, G. C. Trinchero, H. Ulrich, A. Weindl, J. Wochele, M. Wömmmer, and J. Zabierowski, "Kneelike structure in the spectrum of the heavy component of cosmic rays observed with KASCADE-GRANDE," *Phys. Rev. Lett.* **107**, 171104 (2011).
39. B. V. Antokhonov, S. F. Berezhnev, D. Besson, N. M. Budnev, and A. Chiavassa, "TUNKA-133: the new EAS Cherenkov light array for cosmic ray study ( $10^{15}$ – $10^{18}$  eV)," *Proc. Sci. Texas.* **692**, 98 (2010).
40. S. F. Berezhnev, S. N. Epimakhov, N. I. Karpov, N. N. Kalmykov, E. E. Korosteleva, V. A. Kozhin, L. A. Kuzmichev, B. K. Lubsandorzhev, N. B. Lubsan-dorzhev, M. I. Panasyuk, E. G. Popova, V. V. Prosin, V. S. Ptuskin, B. A. Shaibonov, Jr., A. A. Silaev, A. A. Silaev, Jr., A. V. Skurikhin, L. G. Sveshnikova, and I. V. Yashin, "The Tunka-133 EAS Cherenkov light array: status of 2011," *Nucl. Instrum. Methods Phys. Res., A* **692**, 98–105 (2012).
41. J. W. Fowler, L. F. Fortson, C. C. H. Jui, D. B. Kieda, R. A. Ong, C. L. Pryke, and P. Sommers, "A measure-ment of the cosmic ray spectrum and composition at the knee," *Astropart. Phys.* **15** (1), 49–64 (2001).
42. D. V. Chernov, E. E. Korosteleva, L. A. Kuzmichev, V. V. Prosin, I. V. Yashin, N. M. Budnev, O. A. Gress, T. I. Gress, L. V. Pankov, Yu. V. Parfenov, Yu. A. Seme-ney, B. K. Lubsandorzhev, P. G. Pokhil, T. Schmidt, Ch. Spiering, and R. Wischnewski, "Primary energy spectrum and mass composition determined with the TUNKA EAS Cherenkov array," *Int. J. Mod. Phys. A* **20** (29), 6799–6801 (2005).
43. H. Tokuno, F. Kakimoto, S. Ogio, D. Harada, Y. Kurashina, Y. Tsunesada, N. Tajima, Y. Matsubara, A. Morizawa, O. Burgoa, E. Gotoh, K. Kadota, T. Kaneko, M. Kubo, P. Miranda, T. Mizobuchi, Y. Mizumoto, K. Murakami, H. Nakatani, K. Nishi, S. Shimoda, Y. Shirasaki, Y. Toyoda, A. Velarde, K. Yamada, Y. Yamada, and H. Yoshii, "The cosmic ray primary composition at the knee region from lateral

- distributions of atmospheric Cherenkov photons in extensive air showers,” *Astropart. Phys.* **29** (6), 453–460 (2008).
44. Yoshiki Tsunesada, “Cosmic ray observation at mount Chacaltaya for beyond the knee region,” in *Proceedings of 30th ICRC, V. 4, Mexico City, Mexico* (Universidad Nacional Autónoma de México, Merida, 2008), pp. 127–130.
45. W. D. Apel, J. C. Arteaga-Velázquez, K. Bekk, M. Bertina, J. Blümer, H. Bozdog, I. M. Brancus, E. Cantoni, A. Chiavassa, F. Cossavella, K. Daumiller, V. de Souza, F. Di Piero, P. Doll, R. Engel, J. Engler, M. Finger, B. Fuchs, D. Fuhrmann, H. J. Gils, R. Glasstetter, C. Grupen, A. Haungs, D. Heck, J. R. Hörandel, D. Huber, T. Huege, K.-H. Kampert, D. Kang, H. O. Klages, K. Link, P. Łuczak, M. Ludwig, H. J. Mathes, H. J. Mayer, M. Melissas, J. Milke, B. Mitrica, C. Morello, S. Oehlschlager, S. Ostapchenko, N. Palmieri, M. Petcu, T. Pierog, H. Rebel, M. Roth, H. Schieler, S. Schoo, F. G. Schröder, O. Sima, G. Toma, G. C. Trinchero, H. Ulrich, A. Weindl, J. Wochele, M. Wommer, and J. Zabierowski, “Ankle-like feature in the energy spectrum of light elements of cosmic rays observed with KASCADE-Grande,” *Phys. Rev. D* **87**, 081101 (2013).
46. T. Abu-Zayyad, K. Belov, D. J. Bird, J. Boyer, Z. Cao, M. Catanese, G. F. Chen, R. W. Clay, C. E. Covault, H. Y. Dai, B. R. Dawson, J. W. Elbert, B. E. Fick, L. F. Fortson, J. W. Fowler, K. G. Gibbs, M. A. K. Glasmaier, K. D. Green, Y. Ho, A. Huang, C. C. Jui, M. J. Kidd, D. B. Kieda, B. C. Knapp, S. Ko, C. G. Larsen, W. Lee, E. C. Loh, E. J. Mannel, J. Matthews, J. N. Matthews, B. J. Newport, D. F. Nitz, R. A. Ong, K. M. Simpson, J. D. Smith, D. Sinclair, P. Sokolsky, P. Sommers, C. Song, J. K. K. Tang, S. B. Thomas, J. C. van der Velde, L. R. Wiencke, C. R. Wilkinson, S. Yoshida, and X. Z. Zhang, “Measurement of the cosmic-ray energy spectrum and composition from  $10^{17}$  to  $10^{18.3}$  eV using a hybrid technique,” *Astrophys. J.* **557** (2), 686 (2001).
47. Tadeusz Wibig and Arnold W. Wolfendale, “Ultra high energy cosmic rays,” *J. Phys. G: Nucl. Part. Phys.* **34** (9), 1891 (2007).
48. G. Giacinti, M. Kachelrieß, D. V. Semikoz, and G. Sigl, “Cosmic ray anisotropy as signature for the transition from galactic to extragalactic cosmic rays,” *J. Cosmol. Astropart. Phys.* **2012** (07), 031 (2012).
49. (The Pierre Auger Collab.) P. Abreu, M. Aglietta, E. J. Ahn, I. F. M. Albuquerque, D. Allard, I. Allekotte, J. Allen, P. Allison, J. Alvarez Castillo, J. Alvarez-Muñiz, M. Ambrosio, A. Aminaei, L. Anchordoqui, S. Andringa, T. Antičić, C. Aramo, E. Arganda, F. Arqueros, H. Asorey, P. Assis, J. Aublin, M. Ave, M. Avenier, G. Avila, T. Bäcker, M. Balzer, K. B. Barber, A. F. Barbosa, R. Bardenet, S. L. C. Barroso, B. Baughman, J. J. Beatty, B. R. Becker, K. H. Becker, J. A. Bellido, S. Benzi, C. Berat, X. Bertou, P. L. Biermann, P. Billoir, F. Blanco, M. Blanco, C. Bleve, H. Blümer, M. Boháčová, D. Boncioli, C. Bonifazi, R. Bonino, N. Borodai, J. Brack, P. Brogueira, W. C. Brown, R. Bruijn, P. Buchholz, A. Bueno, R. E. Burton, K. S. Caballero-Mora, L. Caramete, R. Caruso, A. Castellina, G. Cataldi, L. Cazon, R. Cesster, J. Chauvin, A. Chiavassa, J. A. Chinellato, A. Chou, J. Chudoba, R. W. Clay, M. R. Coluccia, R. Conceição, F. Contreras, H. Cook, M. J. Cooper, J. Coppens, A. Cordier, U. Cotti, S. Coutu, C. E. Covault, A. Creusot, A. Criss, J. Cronin, A. Curuti, S. Dagoret-Campagne, R. Dallier, S. Dasso, K. Daumiller, B. R. Dawson, R. M. de Almeida, M. De Domenico, C. De Donato, S. J. de Jong, G. De La Vega, W. J. M. de Mello, Jr., J. R. T. de Mello Neto, I. De Mitri, V. de Souza, K. D. de Vries, G. Decerprit, L. del Peral, O. Deligny, H. Dembinski, A. Denkiewicz, C. Di Giulio, J. C. Diaz, M. L. Díaz Castro, P. N. Diep, C. Dobrigkeit, J. C. D’Olivo, P. N. Dong, A. Dorofeev, J. C. dos Anjos, M. T. Dova, D. D’Urso, I. Dutan, J. Ebr, R. Engel, M. Erdmann, C. O. Escobar, A. Etchegoyen, P. Facal San Luis, H. Falcke, G. Farrar, A. C. Fauth, N. Fazzini, A. P. Ferguson, A. Ferrero, B. Fick, A. Filevich, A. Filipčić, S. Fliescher, C. E. Fracchiolla, E. D. Fraenkel, U. Fröhlich, B. Fuchs, R. F. Gamarra, S. Gambetta, B. García, D. García Gámez, D. Garcia-Pinto, A. Gascon, H. Gemmeke, K. Gesterling, P. L. Ghia, U. Giaccari, M. Giller, H. Glass, M. S. Gold, G. Golup, Albarracin. F. Gomez, M. Gómez Berisso, P. Gonçalves, D. Gonzalez, J. G. Gonzalez, B. Gookin, D. Góra, A. Gorgi, P. Gouffon, S. R. Gozzini, E. Grashorn, S. Grebe, N. Griffith, M. Grigat, A. F. Grillo, Y. Guardincerri, F. Guarino, G. P. Guedes, J. D. Hague, P. Hansen, D. Harari, S. Harmsma, J. L. Harton, A. Haungs, T. Hebbeker, D. Heck, A. E. Herve, C. Hojvat, V. C. Holmes, P. Homola, J. R. Hörandel, A. Horneffer, M. Hrabovský, T. Huege, A. Insolia, F. Ionita, A. Italiano, S. Jiraskova, K. Kadija, K. H. Kampert, P. Karhan, T. Karova, P. Kasper, B. Kégl, B. Keilhauer, A. Keivani, J. L. Kelley, E. Kemp, R. M. Kieckhafer, H. O. Klages, M. Kleifges, J. Kleinfeller, J. Knapp, D.-H. Koang, K. Kotera, N. Krohm, O. Krömer, D. Kruppke-Hansen, F. Kuehn, D. Kuempel, J. K. Kulbartz, N. Kunka, G. La Rosa, C. Lachaud, P. Lautridou, M. S. A. B. Leão, D. Lebrun, P. Lebrun, M. A. Leigui de Oliveira, A. Lemiére, A. Letessier-Selvon, I. Lhenry-Yvon, K. Link, R. López, A. Lopez Agüera, K. Louedec, J. Lozano Bahilo, A. Lucero, M. Ludwig, H. Lyberis, C. Macolino, S. Maldera, D. Mandat, P. Mantsch, A. G. Mariazzi, V. Marin, I. C. Maris, H. R. Marquez Falcon, G. Marsella, D. Martello, L. Martin, O. Martínez Bravo, H. J. Mathes, J. Matthews, J. A. J. Matthews, G. Matthiae, D. Maurizio, P. O. Mazur, G. Medina-Tanco, M. Melissas, D. Melo, E. Menichetti, A. Mensehikov, P. Mertsch, C. Meurer, S. Mic’anović, M. I. Micheletti, W. Miller, L. Miramonti, S. Mollerach, M. Monasor, D. Monnier Ragainie, F. Montanet, B. Morales, C. Morello, E. Moreno, J. C. Moreno, C. Morris, M. Mostafá, C. A. Moura, S. Mueller, M. A. Muller, G. Müller, M. Münchmeyer, R. Mussa, G. Navarra, J. L. Navarro, S. Navas, P. Necessal, L. Nellen, A. Nelles, P. T. Nhung, N. Nierstenhoefer, D. Nitz, D. Nosek, L. Nožka, M. Nyklicek, J. Oehlschlager, A. Olinto, P. Oliva, V. M. Olmos-Gilbaja, M. Ortiz, N. Pacheco, D. Pakk Selmi-Dei, M. Palatka, J. Pallotta, N. Palmieri, G. Parente, E. Parizot, A. Parra, J. Parrisius, R. D. Parsons, S. Pastor, T. Paul, M. Pech, J. Pečala, R. Pelayo, I. M. Pepe, L. Perrone, R. Pesce, E. Petermann, S. Petrera, P. Petrinca, A. Petrolini,

- Y. Petrov, J. Petrovic, C. Pfendner, N. Phan, R. Piegai, T. Pierog, P. Pieroni, M. Pimenta, V. Pirronello, M. Platino, V. H. Ponce, M. Pontz, P. Privitera, M. Prouza, E. J. Quel, J. Rautenberg, O. Ravel, D. Ravnani, B. Revenu, J. Ridky, M. Risse, P. Ristori, H. Rivera, C. Rivière, V. Rizi, C. Robledo, W. Rodrigues de Carvalho, G. Rodriguez, J. Rodriguez Martino, J. Rodriguez Rojo, I. Rodriguez-Cabo, M. D. Rodríguez-Frías, G. Ros, J. Rosado, T. Rossler, M. Roth, B. Rouillé-d'Orfeuille, E. Roulet, A. C. Rovero, C. Rühle, F. Salamida, H. Salazar, G. Salina, F. Sánchez, M. Santander, C. E. Santo, E. Santos, E. M. Santos, F. Sarazin, S. Sarkar, R. Sato, N. Scharf, V. Scherini, H. Schieler, P. Schiffer, A. Schmidt, F. Schmidt, T. Schmidt, O. Scholten, H. Schoorlemmer, J. Schovancova, P. Schovánek, F. Schroeder, S. Schulte, D. Schuster, S. J. Scitutto, M. Scuderi, A. Segreto, D. Semikoz, M. Settimo, A. Shadkam, R. C. Shellard, I. Sidelnik, G. Sigl, A. Śmiałkowski, R. Šmída, G. R. Snow, P. Sommers, J. Sorokin, H. Spinka, R. Squartini, J. Stapleton, J. Stasielak, M. Stephan, A. Stutz, F. Suarez, T. Suomijärvi, A. D. Supanitsky, T. Šušar, M. S. Sutherland, J. Swain, Z. Szadkowski, M. Szuba, A. Tamashiro, A. Tapia, O. Taşcau, R. Tcaciuc, D. Tegolo, N. T. Thao, D. Thomas, J. Tiffenberg, C. Timmermans, D. K. Tiwari, W. Tkaczyk, C. J. Todero Peixoto, B. Tomé, A. Tonachini, P. Travnicek, D. B. Tridapalli, G. Tristram, E. Trovato, M. Tueros, R. Ulrich, M. Unger, M. Urban, J. F. Valdés Galicia, I. Valiño, L. Valore, A. M. van den Berg, B. Vargas Cárdenas, J. R. Vázquez, R. A. Vázquez, D. Veberič, V. Verzi, M. Videla, L. Villaseñor, H. Wahlberg, P. Wahrlich, O. Wainberg, D. Warner, A. A. Watson, M. Weber, K. Weidenhaupt, A. Weindl, S. Westerhoff, B. J. Whelan, G. Wieczorek, L. Wiencke, B. Wilczyn'ska, H. Wilczyn'ski, M. Will, C. Williams, T. Winchen, L. Winders, M. G. Winnick, M. Wommer, B. Wundheiler, T. Yamamoto, P. Younk, G. Yuan, B. Zamorano, E. Zas, D. Zavrtnik, M. Zavrtnik, I. Zaw, and A. Zepeda, "Search for first harmonic modulation in the right ascension distribution of cosmic rays detected at the Pierre Auger Observatory," *Astropart. Phys.* **34** (8), 627–639 (2011).
50. D. V. Chernov, R. A. Antonov, E. A. Bonvech, and A. V. Shirokov, "Optical and data acquisition system for the SPHERE-2 detector," in *Proceedings of the 30th ICRC, V. 5, Mexico City, Mexico, 2008*, pp. 941–944.
51. A. M. Anokhina, R. A. Antonov, E. A. Bonvech, V. I. Galkin, T. A. Dzhatdov, A. A. Kirillov, T. M. Roganova, D. V. Chernov, and S. B. Shaulov, "Method for recording spectrum of PCR protons at energies  $>10^{16}$  eV," *Kratk. Soobshch. Fiz.* **36** (5), 32–38 (2009).
52. R. A. Antonov, A. M. Anokhina, E. A. Bonvech, D. V. Chernov, T. A. Dzhatdov, V. I. Galkin, A. A. Kirillov, and T. M. Roganova, "A method for primary proton spectrum measurement at  $E_0 \times 10$  PeV with SPHERE-2 telescope," in *Proceedings of 31st ICRC, V. 4, Lodz, 2009*.
53. V. I. Galkin and T. A. Dzhatdov, "On sensitivity of spatial and angular distribution of Cherenkov light from extensive air showers to the mass composition of primary cosmic rays with energies of  $10^{15}$ – $10^{16}$  eV," *Vestn. Mosk. Univ., Ser. 3: Fiz., Astron., No. 3*, 37–43 (2010).
54. V. I. Galkin and T. A. Dzhatdov, "Separation of PCR nuclear groups with energies of  $10^{15}$ – $10^{16}$  eV using spatial and angular distribution of EAS Cherenkov light," *Izv. Ross. Akad. Nauk, Ser. Fiz.* **75** (3), 338–341 (2011).
55. R. A. Antonov, T. V. Aulova, E. A. Bonvech, S. P. Beschapov, D. V. Chernov, T. A. Dzhatdov, Mir Finger, Mix Finger, V. I. Galkin, N. V. Kabanova, A. S. Petkun, D. A. Podgrudkov, T. M. Roganova, S. B. Shaulov, and T. I. Sysoeva, "First detailed reconstruction of the primary cosmic ray energy spectrum using reflected Cherenkov light," in *Proceedings of 33rd ICRC, 2013*.
56. A. S. Borisov and V. I. Galkin, "Design of a Cherenkov telescope for the measurement of PCR composition above 1 PeV," *J. Phys.: Conf. Ser.* **409** (1), 012089 (2013).
57. A. E. Chudakov, "A possible method of detecting EAS based on Cherenkov radiation reflected from a ground snow surface," in *Proceedings of All-Union Symposium on Experimental Methods of Studying Cosmic Rays with Superhigh Energies, Yakutsk, 1972* (Yakutsk Division, Siberian Branch, USSR Academy of Science, 1974), pp. 69–74.
58. C. Castagnoli, G. Navarra, and C. Morello, "Detection of EAS Cherenkov light reflected from mountain snow," in *Proceedings of 17th International Cosmic Ray Conference, V. 6, Paris, 1981*, p. 103.
59. R. A. Antonov, I. P. Ivanenko, and V. I. Rubtsov, "Installation for measuring to primary energy spectrum of cosmic rays in the energy range above  $10^{15}$ – $10^{16}$  eV," in *Proceedings of 14th ICRC, V. 9, Munich, 1975*, pp. 3360–3363.
60. R. A. Antonov, I. P. Ivanenko, and V. A. Kuz'min, "Mathematical simulation of an experimental setup for studying primary cosmic ray spectrum in the energy range of  $10^{15}$ – $10^{20}$  eV," *Izv. Akad. Nauk SSSR, Ser. Fiz.* **11** (50), 2217–2220 (1986).
61. R. A. Antonov, I. P. Ivanenko, V. A. Kuz'min, and A. N. Fedorov, "Balloon setup for measuring energy spectrum of primary cosmic rays in the energy range from  $10^{15}$  eV to several units of  $10^{20}$  eV," in *Investigations with High-Altitude Balloons. Brief Communications on Physics* (FIAN, Moscow, 1989), pp. 78–81.
62. M. Baranochnikov, *Radiation Receivers and Detectors. Handbook* (DMK Press, Moscow, 2012) [in Russian].
63. Yu. A. Fomin, G. B. Christiansen, G. B. Kulikov, V. G. Pogorely, V. I. Solovjeva, V. P. Sulakov, and A. V. Trubitsyn, "Energy spectrum of cosmic rays at energies of  $5 \times 10^{15}$ – $5 \times 10^{17}$  eV," in *Proceedings of 22nd ICRC, V. 2, Dublin, 1991*, p. 85.
64. M. Teshima, "Origin of cosmic rays above  $10^{14}$  eV. Rapporteur," in *Proceedings of 23rd Int. Cosmic Ray Conference, V. 3, Calgary, 1993*, p. 257.
65. L. I. Vil'danova, P. A. Dyatlov, and N. M. Nesterova, "Energy spectrum of primary cosmic rays and its specific features at energies above  $10^{18}$  based on data on EAS spectrum from a number of electrons at the Tien Shan level," *Izv. Ross. Akad. Nauk, Ser. Fiz.* **12** (58), 79 (1994).
66. Toirkhon Alimov, "Study of energy spectrum of primary cosmic rays in the energy range of  $10^{15}$ – $10^{16}$  eV,"

- Candidate's Dissertation in Mathematical Physics (Leningrad Polytechnic Inst., Leningrad, 1985).
67. A. V. Glushkov, N. N. Efimov, T. A. Egorov, N. N. Efremov, and S. P. Knurenko, "Cosmic ray spectra measurements at the Yakutsk EAS array," in *Proceedings of 19th ICRC, La Jolla, 1985*, p. 198.
  68. M. N. Dyakov, N. N. Efimov, T. A. Egorov, N. N. Efremov, and S. P. Knurenko, "Primary energy spectrum of cosmic rays with  $E_0 \approx 10^{16}$ – $10^{20}$  eV on data of the Yakutsk array," in *Proceedings of 22nd ICRC, V. 2, Dublin, 1991*, p. 93.
  69. M. A. Lawrence, R. J. O. Reid, and A. A. Watson, "The cosmic ray energy spectrum above  $4 \times 10^{17}$  eV as measured by the Haverah Park array," *J. Phys. G: Nucl. Part. Phys.* **17** (5), 733 (1991).
  70. G. L. Cassiday, R. Cooper, S. C. Corbato, B. R. Dawson, J. W. Elbert, B. E. Fick, K. D. Green, D. B. Kieda, S. Ko, E. C. Lon, M. H. Salamon, J. Smith, P. Sokolsky, S. B. Thomas, and B. M. Wheeler, "The ultra high energy cosmic ray spectrum," in *Proceedings of 21st ICRC, V. 3, Adelaide, Australia, 1990*, p. 163.
  71. D. J. Bird, S. C. Corbató, H. Y. Dai, B. R. Dawson, J. W. Elbert, B. L. Emerson, M. A. Huang, D. B. Kieda, M. Luo, S. Ko, C. G. Larsen, E. C. Loh, M. H. Salamon, J. D. Smith, P. Sokolsky, P. Sommers, J. K. K. Tang, and S. B. Thomas, "The Fly's Eye extremely high energy cosmic ray spectrum," in *Proceedings of 23rd ICRC, V. 2, Calgary, 1993*, p. 34.
  72. R. A. Antonov, E. A. Petrova, and A. N. Fedorov, "Measurement of energy spectrum of primary cosmic rays at energies  $> 10^{16}$  eV by the method of detecting EAS Cherenkov light reflected from a snow surface," Preprint No. 95-4/368 (Skobel'syn Inst. of Nuclear Physics, Moscow State Univ., Moscow, 1995).
  73. A. N. Fedorov, "Measurement of energy spectrum of primary cosmic rays at energies  $> 10^{16}$  eV by the method of detecting EAS Cherenkov light reflected from a snow surface," Dissertation (Skobel'syn Inst. of Nuclear Physics, Moscow State Univ., Moscow, 1996).
  74. R. A. Antonov, E. A. Petrova, T. I. Sysoeva, A. N. Fedorov, and D. V. Chernov, "Measurement of PCR energy spectrum in the energy range of 10–100 PeV using the SPHERE balloon setup," *Izv. Ross. Akad. Nauk, Ser. Fiz.* **63** (3), 520–524 (1999).
  75. I. Veinberg, *Catalogue of Colored Glass* (Mashinostroenie, Moscow, 1967) [in Russian].
  76. R. A. Antonov, D. V. Chernov, E. E. Korosteleva, T. I. Sysojeva, and W. Tkaczyk, "Balloon-borne measurements of the CR energy spectrum in the energy range 10–100 PeV," in *Proceedings of 27th ICRC, V. 1 (Copernicus Gesellschaft, Hamburg, 2001)*, pp. 59–62.
  77. E. A. Petrova, "Method of measuring energy spectrum of primary cosmic rays at energies above  $10^{16}$  eV using the SPHERE balloon setup," Candidate's Dissertation in Mathematical Physics (Skobel'syn Inst. of Nuclear Physics, Moscow State Univ., Moscow, 1998).
  78. N. M. Budnev, R. V. Vasil'ev, O. A. Gress, T. I. Gress, E. E. Korosteleva, L. A. Kuz'michev, B. K. Lubsandorzhev, A. I. Panfilov, L. V. Pan'kov, Yu. V. Parfenov, V. V. Prosin, P. G. Pokhil, T. Shmidt, K. Shpiring, Yu. A. Semenei, D. V. Chernov, and I. V. Yashin, "Energy spectrum of primary cosmic rays around a 'knee' according to data of the Tunka-25 setup for studying Cherenkov radiation," *Izv. Ross. Akad. Nauk, Ser. Fiz.* **66** (11), 1563 (2002).
  79. M. P. D'yakonov, N. N. Efimov, S. R. Knurenko, V. A. Kolosov, E. S. Nikiforova, S. I. Nikol'skii, V. V. Prosin, I. E. Sleptsov, G. G. Struchkov, and G. B. Christiansen, "Function of spatial distribution of Cherenkov light from extensive air showers at energies from  $7 \times 10^{15}$  to  $3 \times 10^{19}$  eV," *Izv. Ross. Akad. Nauk, Ser. Fiz.* **57** (4), 86–90 (1993).
  80. WaveJet 300A Oscilloscopes 100 MHz–500 MHz: Datasheet: WJADS-12feb13 / Teledyne LeCroy; Executor: Teledyne LeCroy: 2012.
  81. Hamamatsu Photonics. Photomultiplier Tubes and related products. Product catalog. Japan, 2010. Nov. TPMZ0001E01.
  82. CORSIKA: A Monte Carlo Code to Simulate Extensive Air Showers: Wissenschaftliche Berichte: FZKA 6019 / Forschungszentrum Karlsruhe; Executor: D. Heck, J. Knapp, J. N. Capdevielle, et al. (1998).
  83. N. N. Kalmykov and S. S. Ostapchenko, "Nucleus–nucleus interaction, fragmentation of nuclei, and fluctuations in extensive air showers," *Yad. Fiz.* **3**, 105–119 (1993).
  84. N. N. Kalmykov, S. S. Ostapchenko, and A. I. Pavlov, "Quark-gluon-string model with allowance for jets and EAS," *Izv. Ross. Akad. Nauk, Ser. Fiz.* **58** (12), 21–25 (1994).
  85. N. N. Kalmykov, S. S. Ostapchenko, and A. I. Pavlov, "Quark-gluon-string model and EAS simulation problems at ultra-high energies," *Nucl. Phys. B, Proc. Suppl.* **52** (3), 17–28 (1997).
  86. S. Ostapchenko, "QGSJET-II: towards reliable description of very high energy hadronic interactions," *Nucl. Phys. B, Proc. Suppl.* **151** (1), 143–146 (2006).
  87. S. Ostapchenko, "Nonlinear screening effects in high energy hadronic interactions," *Phys. Rev. D* **74** (1), (2006).
  88. GHEISHA program: Technical Report PITHA: 85-02/III Physikalisches Institut, RWTH Aachen Physikalische Institut; Executor: H. C. Fesefeldt (1985).
  89. T. A. Dzhatdov, "Multidimensional criteria for reconstructing mass composition of primary cosmic rays based on the parameters of EAS Cherenkov light," Candidate's Dissertation in Mathematical Physics (Skobel'syn Inst. of Nuclear Physics, Moscow State Univ., Moscow, 2011).
  90. M. Born and E. Wolf, *Principles of Optics* (Pergamon, Oxford, 1969; Nauka, Moscow, 1973).
  91. R. A. Antonov, S. P. Beschapov, E. A. Bonvech, D. V. Chernov, T. A. Dzhatdov, Mir. Finger, Mix. Finger, V. I. Galkin, N. V. Kabanova, A. S. Petkun, D. A. Podgrudkov, T. M. Roganova, S. B. Shaulov, and T. I. Sysoeva, "Results on the primary CR spectrum and composition reconstructed with the SPHERE-2 detector," *J. Phys.: Conf. Ser.* **409** (1), 012088–012091 (2013).
  92. S. Agostinelli, J. Allison, K. Amako, J. Apostolakis, H. Araujo, P. Arce, M. Asai, D. Axen, S. Banerjee, G. Barrand, F. Behner, L. Bellagamba, J. Boudreau, L. Broglia, A. Brunengo, H. Burkhardt, S. Chauvie,

- J. Chuma, R. Chytraccek, G. Cooperman, G. Cosmo, P. Degtyarenko, A. Dell'Acqua, G. Depaola, D. Dietrich, R. Enami, A. Feliciello, C. Ferguson, H. Fesefeldt, G. Folger, F. Foppiano, A. Forti, S. Garelli, S. Giani, R. Giannitrapani, D. Gibin, J. J. Gómez Cadenas, I. González, G. Gracia Abril, G. Greeniaus, W. Greiner, V. Grichine, A. Grossheim, S. Guatelli, P. Gumplinger, R. Hamatsu, K. Hashimoto, H. Hasui, A. Heikkinen, A. Howard, V. Ivanchenko, A. Johnson, F. W. Jones, J. Kallenbach, N. Kanaya, M. Kawabata, Y. Kawabata, M. Kawaguti, S. Kelner, P. Kent, A. Kimura, T. Kodama, R. Kokoulin, M. Kossov, H. Kurashige, E. Lamanna, T. Lampén, V. Lara, V. Lefebure, F. Lei, M. Liendl, W. Lockman, F. Longo, S. Magni, M. Maire, E. Medernach, K. Minamimoto, P. Mora de Freitas, Y. Morita, K. Murakami, M. Nagamatu, R. Nartallo, P. Nieminen, T. Nishimura, and K. Ohtsubo, M. Okamura, S. O'Neale, Y. Oohata, K. Paech, J. Perl, A. Pfeiffer, M. G. Pia, F. Ranjard, A. Rybin, S. Sadilov, E. Di Salvo, G. Santin, T. Sasaki, N. Savvas, Y. Sawada, S. Scherer, S. Sei, V. Sirotenko, D. Smith, N. Starkov, H. Stoecker, J. Sulkimo, M. Takahata, S. Tanaka, E. Tcherniaev, Tehrani, E. Safai, M. Tropeano, P. Truscott, H. Uno, L. Urban, P. Urban, M. Verderi, A. Walkden, W. Wander, H. Weber, J. P. Wellisch, T. Wenaus, D. C. Williams, D. Wright, T. Yamada, H. Yoshida, and D. Zschiesche, *Nucl. Instrum. Methods Phys. Res., A* **506** (3), 250–303 (2003).
93. S. Over and M. Grumpert, “Search for anisotropy and point sources of cosmic rays with the KASCADE-Grande experiment,” in *Proceedings of 30th ICRC, V. 4, Mexico City, Mexico* (Universidad Nacional Autónoma de México, Merida, 2008), pp. 223–226.
94. L. G. Dedenko, G. F. Fedorova, E. Yu. Fedunin, A. V. Glushkov, V. A. Kolosov, D. A. Podgrudkov, M. I. Pravdin, T. M. Roganova, and I. E. Slepsov, “Energy estimation of inclined air showers with help of detector responses,” *Nucl. Phys. B, Proc. Suppl.* **136**, 12–17 (2004).
95. W. D. Apel, J. C. Arteaga-Velázquez, K. Bekk, M. Bertina, J. Blüamer, H. Bozdog, I. M. Brancus, E. Cantoni, A. Chiavassa, F. Cossavella, K. Daumiller, V. de Souza, F. Di Pierro, P. Doll, R. Engel, J. Engler, M. Finger, B. Fuchs, D. Fuhrmann, H. J. Gils, R. Glasstetter, C. Grupen, A. Haungs, D. Heck, J. R. Hörandel, D. Huber, T. Huege, K.-H. Kampert, D. Kang, H. O. Klages, K. Link, P. Łuczak, M. Ludwig, H. J. Mathes, H. J. Mayer, M. Melissas, J. Milke, B. Mitrica, C. Morello, J. Oehlschläger, S. Ostapchenko, N. Palmieri, M. Petcu, T. Pierog, H. Rebel, M. Roth, H. Schieler, S. Schoo, F. G. Schröder, O. Sima, G. Toma, G. C. Trinchero, H. Ulrich, A. Weindl, J. Wochele, M. Wömmmer, and J. Zabierowski, “KASCADE-Grande measurements of energy spectra for elemental groups of cosmic rays,” *Astropart. Phys.* **47**, 54–66 (2013).

*Translated by A. Sin'kov*